Study of proximity effect in YBCO/FePd heterostructures

Master thesis

by Mengying Tang from RWTH

at the Jülich Centre for Neutron Science, Institute of Quantum Materials
and Collective Phenomena
in Forschungszentrum Jülich

supervised by
Prof. Dr. Thomas Brückel
Prof. Dr. Joachim Mayer

advised by
Dr. Emmanuel Kentzinger
Dr. Connie Bednarski-Meinke
Prof. Dr. Michael Faley

01. August 2022 – 19. June 2023

1 Introduction

The generation of domain wall superconductivity and spin-triplet state Cooper pairs in ferromagnets with large penetration depths could play an important role for the development of spintronic devices and quantum computing applications. In the heterostructures of multilayer films, the proximity effect is closely related to the interfacial electronic states. Based on the results of my project thesis : Perovskite $YBa_2Cu_3O_{7-x}$(YBCO) and FePd were used in the heterostructure of HTS/F (high temperature superconductor /ferromagnet) because of their well-matched lattice constants: in-plane lattice constants of YBCO are a=3.823Å and b=3.88Å and of FePd is a=b=3.849Å. However, the innate spiral pattern on the growth surface of YBCO, and technological incompatibility of the growth conditions for epitaxial FePd, makes the realization of such a heterostructure very difficult. The superconducting state of YBCO is highly sensitive to its oxidation state, however, among the HTS/F heterostructures formed by depositing FePd on YBCO, deposition by shuttered growth at room temperature was determined to have the least effect on the superconducting state of YBCO. Therefore, the HTS/F heterostructure samples in this work were prepared by shuttered deposition at room temperature and were further investigated in terms of electronic transport properties. The electronic transport properties are examined for indication of proximity effects.

2 Theoretical Background

2.1 Ferromagnetism

The perpendicular magnetic anisotropy (PMA) of thin films has attracted a lot of interest in the last decade because of its possible applications in magnetic recording, magneto-optical recording and patterned media [1]. When the material is in the form of a thin film, magnetic domain analysis is particularly important to provide a deeper understanding of the relationship between microstructure and magnetic anisotropy in magnetic materials [2].

In this section, the basics of ferromagnetism, magnetic domain, magnetic anisotropy and $L1_0$-phase FePd are discussed.

2.1.1 The Basics of Ferromagnetism

After a ferromagnetic material is magnetized by an external magnetic field, it maintains its magnetized state and remains magnetic even when the external magnetic field is removed, which is known as spontaneous magnetization. This is attributed to the exchange interactions between electrons, which can be described by the Heisenberg model, so ferromagnetism can be well modeled by the Heisenberg model [3].

If the wave functions of two electrons overlap, then the Pauli exclusion principle is to be followed in the overlapping region, i.e., the spins must be antisymmetric when the orbital wave functions are symmetric. The interrelationship of the two electron spins is as follows (2.1):

$$\mathcal{H}_{\mathrm{Heis}} =- 2\mathrm{J} \cdot \overrightarrow{\mathrm{S}_1} \cdot \overrightarrow{\mathrm{S}_2} \qquad (2.1)$$

Equation (2.1) summarizes the conditions required to lead to a magnetically ordered state. Thus, when the exchange integral $\mathrm{J} > 0$ produces ferromagnetism then, $\mathrm{J} < 0$ produces antiferromagnetism [d]. In many cases, only the closest neighboring interactions need to be considered, so a greatly simplified Heisenberg Hamiltonian can be obtained. The Hamiltonian of the Heisenberg model with an external applied magnetic field $\mu_0 \overrightarrow{\mathrm{H}}_{\mathrm{ext}}$ is given by (2.2):

$$\mathcal{H} =- \sum_{i,j} \mathrm{J}_{i,j} \overrightarrow{\mathrm{S}_i} \cdot \overrightarrow{\mathrm{S}_j} + \mathrm{g}\mu_{\mathrm{B}} \sum_{j} \overrightarrow{\mathrm{S}_j} \cdot \mu_0 \overrightarrow{\mathrm{H}}_{\mathrm{ext}} \qquad (2.2)$$

Here, $\mathrm{J}_{\mathrm{i,j}}$ is the exchange coupling constant between the spins on sites i^{th} and j^{th}. In ferromagnetic materials, the electron spins tend to align in parallel, so $\mathrm{J}_{\mathrm{i,j}} > 0$. g is the Landé g factor, and μ_{B} is the Bohr magneton.

In metallic ferromagnets, the magnetic properties are mainly determined by the conduction band electrons, so the energy band theory of ferromagnetism applies. Since the magnetic moment can only come from unpaired electrons, all electron spins in a completely filled energy band are paired, so they cannot contribute to the magnetic moment. The exchange energy lifts the degeneracy of spin-up and spin-down sub-bands, and sub-band splitting occurs. The larger the exchange energy, the larger the energy difference between the two sub-bands. The electrons will preferentially occupy the lower energy level when filling, and when the energy level is split as in Fig. 2.1, the electrons start filling the spin-down sub-band before they completely fill the spin-up sub-band, which results in a non-integer magnetic moment for each atom.

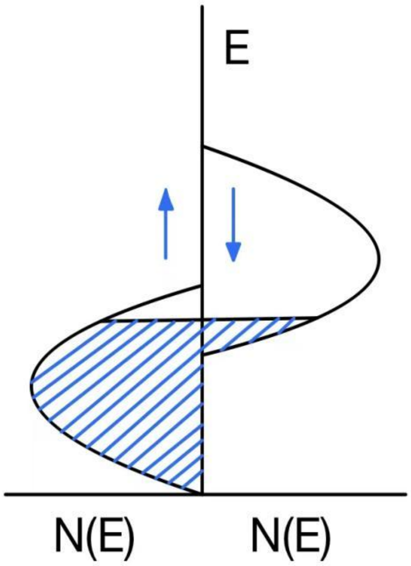

Figure 2.1: Schematic diagram of the energy band structure density of states, showing spin-up and spin-down band splitting. The figure is adapted from [4].

It is necessary to mention hysteresis to describe the basic magnetic properties of a ferromagnet, which is the variation of the magnetic induction B or magnetization strength M for different magnetic field strengths H. A typical hysteresis line is shown in Fig. 2.2.

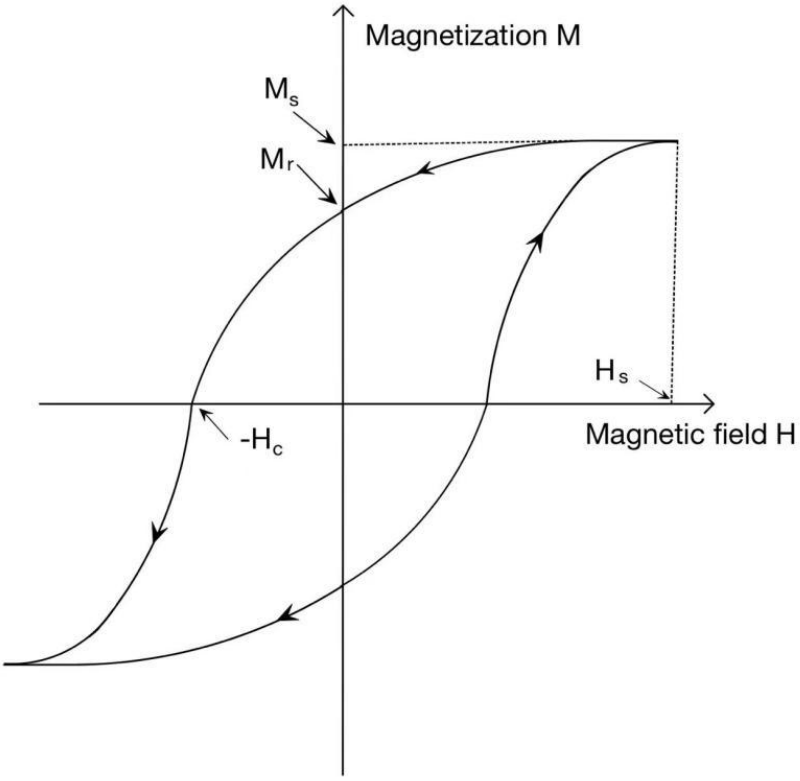

Figure 2.2: Magnetic hysteresis loop of a ferromagnetic material. The figure is adapted from [5].

By applying an external magnetic field, the ferromagnetic material will be highly magnetized in a direction parallel to the external field. The magnetization will increase with the applied magnetic field, but non-linearly, until the saturation magnetization strength M_s is reached. When the applied magnetic field exceeds the saturation magnetic field strength H_S, the magnetization keeps constant because all magnetic moments in the ferromagnet are already aligned in a direction parallel to the external magnetic field. When the magnetic field decreases from $+H_S$ to zero, there is still some remaining magnetization strength M_r existing inside the material. In order to bring the magnetization to zero, a critical field H_C (coercive field) in the opposite direction must be applied. Magnetic materials are classified into hard and soft magnetic materials according to their coercive field. Materials with a coercivity greater than 125 Oe (10K A/m) are defined as hard magnetic materials [4]. While soft magnetic materials have small coercive field and high magnetic susceptibility, which are easy to magnetize and demagnetize. Their main functions are magnetic conductivity, electromagnetic energy conversion and transmission [4].

2.1.2 Magnetic Domains

The presence of magnetic domains causes the hysteresis phenomenon in ferromagnets. The local magnetization strength of each tiny magnetic domain is saturated. The area at the boundary of the domain is the "domain wall", which separates the different domains and has different properties from the rest of the domain. Therefore, understanding the variation of the domain walls is an essential step in describing the magnetization process.

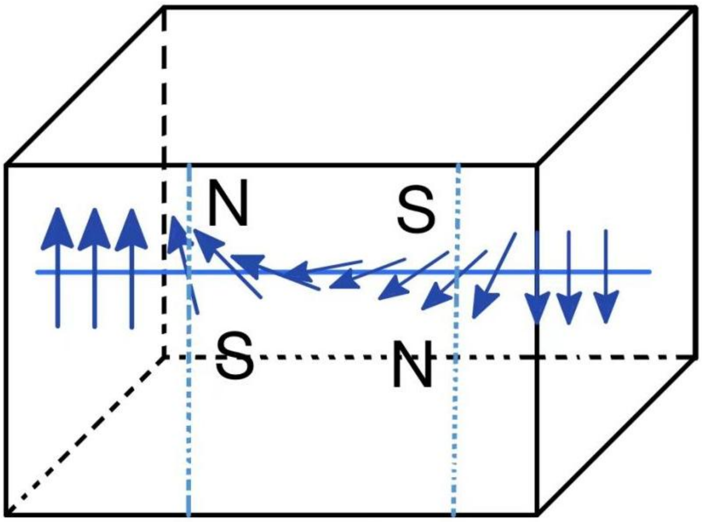

Figure 2.3: 180° arrangement of individual magnetic moments within the domain walls, the figure is adapted from [6].

According to the magnetic domain theory, the ferromagnet is also ordered in the demagnetized state [4]. Applying a magnetic field to a demagnetized ferromagnet, at low fields, the domains oriented in the direction of the magnetic field grow and the size of the domains in the opposite direction decreases, as in Fig. 2.4 (b). At medium field strength a rotation of the magnetic domains occurs, and the atomic magnetic moments in the reversed domains overcome the anisotropy and their direction shifts from the original magnetization direction to one of the easily magnetized crystallographic axes closest to the direction of the external magnetic field, as shown in Fig. 2.4 (c). Eventually, at high fields, the magnetic moments of all easily magnetized crystalline axes orientations gradually turn to the magnetic field direction, as in Fig.2.4 (d).

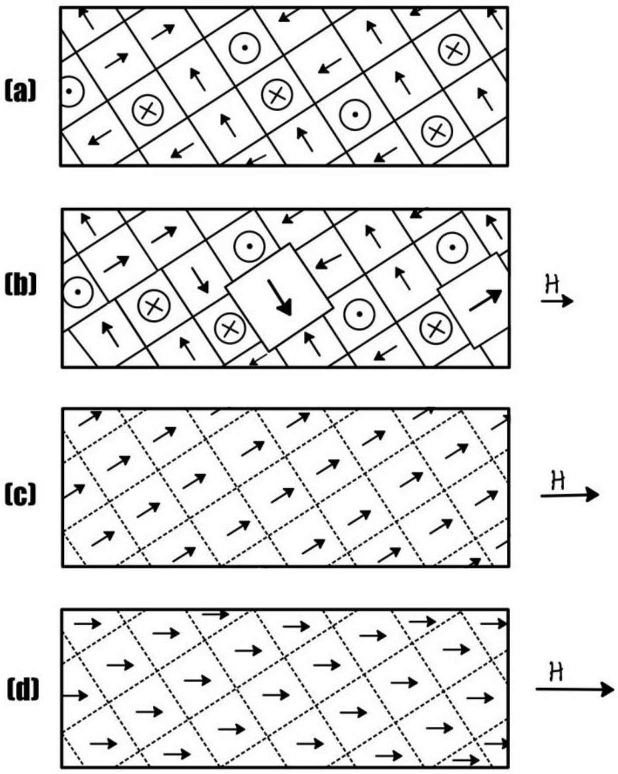

Figure 2.4: Magnetic domains change process of material magnetization until saturation. The figure is adapted from [4].

Figure 2.5 gives the gradual appearance of magnetic domains in the demagnetized state of a sample initially in saturation. As shown in Fig. 2.5 (a) starting from the single domain state, (b)-(d) the domain walls start to form gradually and the total magnetic energy of the film is also gradually decreasing. The final size and shape of the magnetic domains are determined by the competition between the static magnetic energy and anisotropy [5].

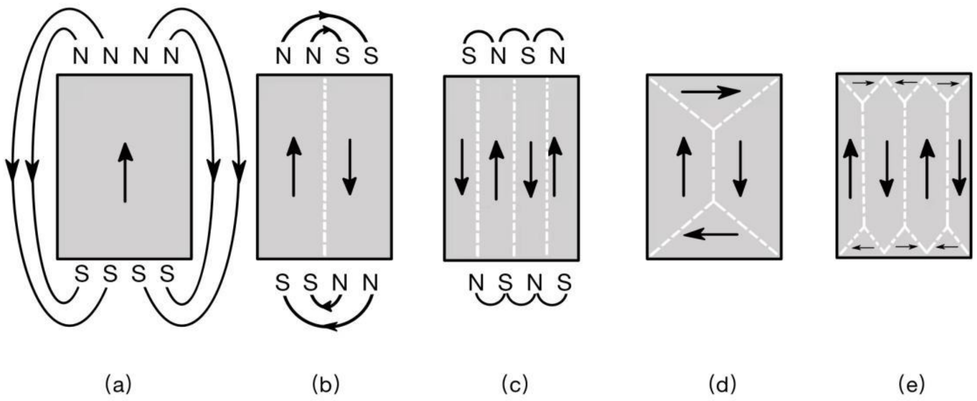

Figure 2.5: The origin of magnetic domains due to magnetostatic energy. The figure is adapted from [5].

2.1.3 Magnetic Anisotropy

Magnetic anisotropy is the phenomenon that the magnetic properties of a material change with direction. It is mainly reflected in the magnetization rate of weak magnets and the magnetization curve of a ferromagnet that changes with the direction of magnetization. In this section, ferromagnet is focused on, where the magnetic anisotropy is particularly prominent, as shown by the saturation (or spontaneous) magnetization with different free energy densities at different crystal orientations. There is an easy magnetization axis in ferromagnetic materials, and the material is easily magnetized along this direction. Magnetic anisotropy originates from the magnetocrystalline anisotropy [6].

Magnetic crystal anisotropy refers to the different magnetization curves of strong magnets when magnetized along different crystal axes. There are several microscopic mechanisms for the anisotropic properties of magnetic crystals [6]: (i) Magnetic dipole interactions: classical magnetic dipole interaction can cause anisotropy only for non-cubic crystals. However, the contribution is usually small. (ii) Anisotropic exchange interactions: the electron spin is related to the orbital angular momentum, which is achieved through the interaction of the spin-magnetic moment with the lattice. In crystals, the electrostatic potential of the lattice affects the orbital angular momentum. This causes the orbital angular momentum of some crystal axes to be biased towards other crystal axes, and this asymmetry carries over to the corresponding crystal axes. In the case of crystal asymmetry (e.g., amorphous ferromagnetic materials), the magnetic crystal anisotropy disappears. However, polycrystalline films can also have a small magnetocrystalline anisotropy due to the uniform distribution of randomly oriented particles on the macroscopic scale [7]. (iii) Single ion anisotropy: the combined effect of crystal electric field and orbital-spin interaction. It makes the energy levels of individual ions anisotropic. For ferrite and some rare earth ions, the contribution is dominant. (iv) Itinerant electron anisotropy: from the effect of orbital-spin interaction on energy bands. This applies to 3d metals and alloys.

For single-domain particles with uniaxial anisotropy, the magnetocrystalline anisotropy energy of the magnetization distributed along the easy axis is given by (2.3).

$$\mathrm{E_{ma}} = \mathrm{KV} \cdot sin^2 \theta \tag{2.3}$$

Here, K is the magnetocrystalline anisotropy constant, θ is the angle between the magnetization and easy axis [3].

2.1.4 $L1_0$-FePd

The $L1_0$-type structure of FePd is ferromagnetic and has significant mechanical and high perpendicular magnetic anisotropy (PMA) with the tetragonal c-axis of the ordered domains as the ‘‘easy axis’’ of magnetization [8].

Figure 2.6 shows AFM images of FePd films grown at different temperatures. The FePd films grown at different temperatures have different structures. In Annika Stellhorn's paper [3], there are two points about the growth of FePd: (i) samples with low PMA can be grown at room temperature using the shuttered-deposition (mimicking a layer by layer growth mode). (ii) the ordered $L1_0$-phase can be obtained at high temperature (600K) using the co-deposition growth mode. As the substrate temperature increases, FePd tends to nucleate in 3D-islands, forming large islands with small planes that are tilted with respect to the substrate surface. Thus, it can be speculated that the 2D-3D growth mode shift found in the sample and the mixture of $L1_0$-phase and fcc hinder the long range order and prevent further chemical ordering [8]. The degree of order increases with the increase of substrate temperature. The magnetic properties are influenced by the crystal orientation and the degree of ordering of the $L1_0$ crystals [9].

To observe and measure the proximity effect, ferromagnetic thin films with high PMA are the ideal material, however, as concluded in my project thesis: heating the substrate is a necessary condition when using the co-deposition growth mode, and the very tricky point is that YBCO is very temperature sensitive in an oxygen-free environment. Heating the substrate will cause YBCO to lose oxygen and thus reduce the superconductivity of YBCO. Therefore, in this study, the shuttered-deposition at room temperature is our compromise choice in order to ensure the loss of superconductivity of YBCO is minimized.

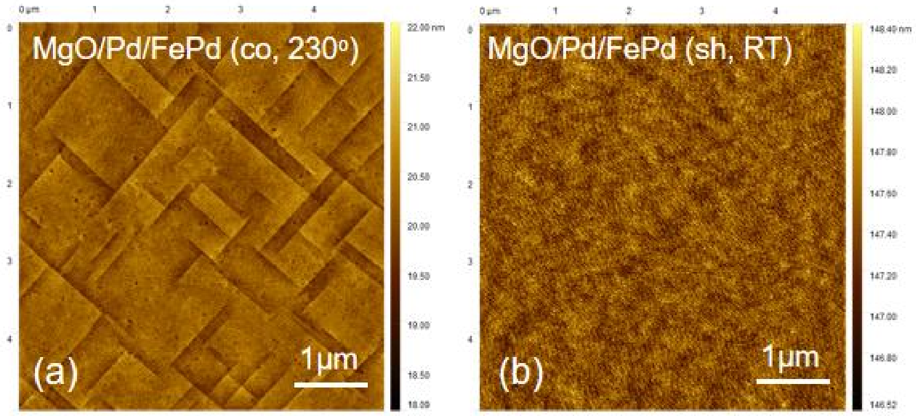

Figure 2.6: AFM images of FePd samples: (a) FePd with terraces was grown at 230℃ in co-deposition growth mode and (b) FePd was grown at room temperature in shuttered-deposition.

2.2 Superconductivity

In 1908, the Dutch physicist Heike Kamerlingh-Onnes succeeded in liquefying helium, and then in the spring of 1911, at the Leiden laboratory, H. Kamerlingh-Onnes found that the resistance of mercury suddenly dropped to zero when the temperature of mercury was lowered to 4.15 K with liquid helium [5]. When the temperature of a specimen is dropped low enough, many metals and alloys suddenly have zero resistivity, a phenomenon known as superconductivity [10]. In this section, we will outline the nature of superconductivity, the most important theoretical models describing superconductivity and give a brief description of the structure of the type II superconductor used in this work, YBCO.

2.2.1 Properties of superconductivity

2.2.1.1 Perfect conductivity

The resistivity of ordinary conductors such as silver and copper also gradually decreases with temperature, but not indefinitely, as they also show some residual resistance. However, when superconductors such as Sn and Nb cool below a specific temperature T_C and change to a superconducting state, their DC resistivity suddenly drops to zero or close to zero, which leads to a continuous undecayed current observed in a ring of the superconducting material. The finite decay time of superconducting materials was observed by File and Mills due to the irreversible redistribution of the magnetic flux in the superconducting material. They studied the decay of supercurrents, using precision NMR methods to measure the associated magnetic fields, which led to the conclusion that the decay time of supercurrents is no less than 100,000 years [5]. This phenomenon is known as perfect conductivity.

As shown in Figure 2.7 (a), the superconductivity transition temperature (or critical temperature, T_C) is the external temperature corresponding to when the resistance suddenly drops to zero. Both heating ($T>T_C$) and the applying a magnetic field (critical field of H_{cm}) can destroy superconductivity. H_{cm} is temperature dependent and can be described by equation (2.4):

$$H_{cm} = H_{cm}(0)\left[1 - (\frac{T}{T_c})^2\right] \tag{2.4}$$

2.2.1.2 Perfect diamagnetism

When the temperature drops below T_C, a superconducting state is formed, then the superconductor has zero magnetic field inside under a weak magnetic field (i.e. $H_{ext} < H_{cm}$). By placing a conductor directly in a weak magnetic field and then slowly cooling it, the initial magnetic flux present inside the conductor is ejected when the temperature falls below T_C, which is known as the Meissner-Ochsenfeld effect [5]. The inherent property of the superconducting state is that it is ideally diamagnetic. Also, it has been proven that the superconducting leap is a phase transition [5].

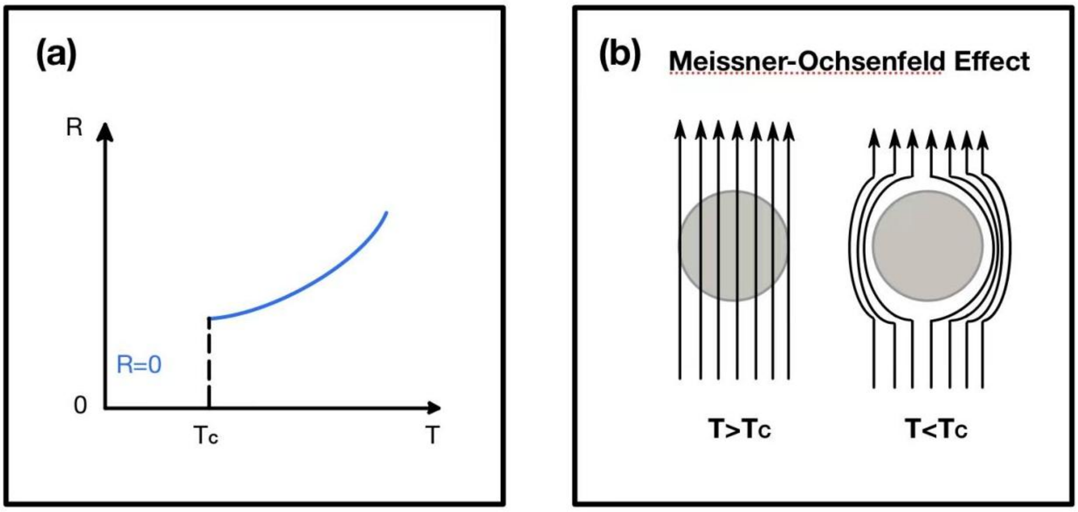

Figure 2.7: Properties of superconductivity. (a)Zero resistance (perfect conductivity). For T < T_C, the superconductor has a perfect conductivity with zero resistance. (b) Meissner-Ochsenfeld effect (ideal diamagnetism). When temperatures T > T_C, the magnetic field B penetrates the superconductor, whereas for T < T_C, the magnetic field B is excluded from the superconductor. The figure is adapted from [12].

2.2.1.3 Type-II superconductors

The different states produced by superconductors due to different applied magnetic fields can be classified into two types of superconductors according to the different states.

Type I superconductors as shown in Fig.2.8 (a), formerly known as soft superconductors, have perfect diamagnetic properties when the applied magnetic field is less than H_{cm}.

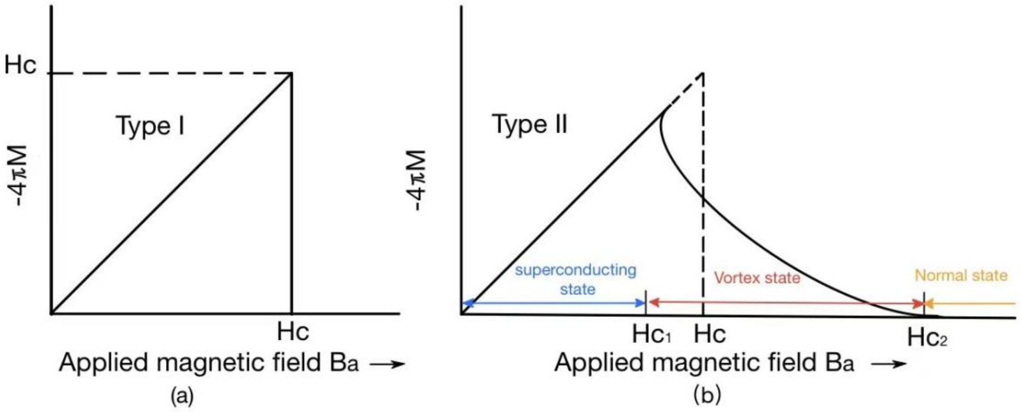

Figure 2.8: Two types of Superconductors.

Type II superconductors tend to be alloys or transition metals with high resistivity in the normal state [5]. When the applied magnetic field is lower than the lower critical field H_{c1}, they exhibit perfect diamagnetism as type I superconductors. However, when external magnetic field H is higher than H_{C1} and lower than the upper critical magnetic field H_{C2}, the superconductor is in a mixed state where the magnetic flux density B is not equal to zero. In this intermediate state, the superconductor is crossed by flux lines in the form of quantum vortices (Figure 2.9). Each vortex has a quantum of magnetic flux Φ_0. As the applied magnetic field increases, the quantum vortices become more and more numerous, and superconductivity will be broken when the vortex density is sufficiently high at $H>H_{C2}$.

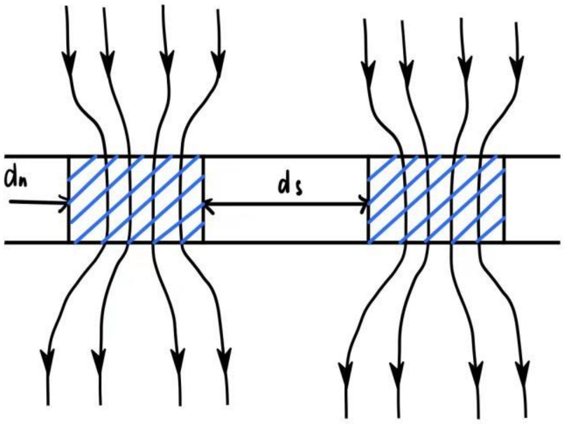

Figure 2.9: Intermediate state (mixed state) of a thin superconducting layer with a perpendicular field; With d_s being the width of a superconducting region and d_n as the width of a normal region. The figure is adapted from [10].

2.2.2 BCS theory

BCS theory is a microscopic theory that explains the superconductivity of superconductors. It has a wide range of applicability, from He^3 atoms in condensed phases, to type I and type II metallic superconductors [5].

The BCS theory explains the superconductivity in metals. Electrons pass through the lattice while attracting a positive charge from a neighboring lattice point. The separation of the ground state from the excited state by an energy gap is due to the attractive interaction between the electrons. The presence of the energy gap leads to critical fields, thermal properties and most of the electromagnetic properties [11]. The electron-lattice electron interaction triggers an energy gap of a size that can be observed. When one electron interacts with the lattice and causes a local deformation of the lattice point, a localized region of high positive charge is formed. This localized region of high positive charge in turn attracts electrons with opposite spin and momentum. A second electron encounters the deformed lattice and adjusts itself to reach the lowest energy. Thus, the second electron interacts with the first electron by lattice deformation and pairs up. This binding energy may be higher than the energy of the lattice atom vibrations when the temperature is below the critical temperature. Therefore, the electron pair does not exchange energy with the lattice, so there is no resistance, resulting in so-called "superconductivity". Two electrons with opposite spin and momentum are coupled at $T < T_C$ and then form a Cooper pair (CP).

2.2.3 Ginzburg-Landau theory

In Ginzburg-Landau theory (G-L theory), Ginzburg and Landau decided to consider an effective wavefunction of the superconducting electrons $\Psi(\mathrm{r})$ as an order parameter. The macroscopic wave function can be described by the local density of Cooper pairs (CPs):

$$|\Psi|^2 = \frac{n_s}{2} \tag{2.5}$$

With n_s being the local density of the superconducting electrons.

The expansion of free energy F of a superconducting condensate is given by:

$$F = F_n + \alpha|\Psi|^2 + \frac{\beta}{2}|\Psi|^4 + \frac{1}{2m^*}\left|-i\hbar\nabla\Psi - \frac{2e}{c}A\Psi\right|^2 + \frac{H^2}{8\pi} \tag{2.6}$$

With the free energy in the normal state F_n, the electron mass m, charge e, the magnetic energy density $H^2/8\pi$, and the exact microscopic field at a given point of the superconductor H. The forth term is the kinetic energy density of the superconducting electrons [10].

By calculating $\boldsymbol{j_s} = -\delta F[\Psi, A]/\delta A(r)$, the second equation of Ginzburg-Landau theory can be obtained:

$$\boldsymbol{j}_s = -\frac{i\hbar e}{2m}(\Psi^*\nabla\Psi - \Psi\nabla\Psi^*) - \frac{2e^2}{mc}|\Psi|^2\mathbf{A} \qquad (2.7)$$

Where A is the vector potential, $\boldsymbol{j}_s$ is the current density in the superconductor. In addition, with Maxwell's equation and $\Psi_0{}^2 = n_s/2 = |\alpha|/\beta$, two more definitions will be introduced [10]:

Coherence length ξ describe the correlation length between two electrons of a Cooper pair in a superconductor, in other words, the distance that the Cooper electron pair extends in space:

$$\xi = \sqrt{\frac{\hbar^2}{2m|\alpha|}} \qquad (2.8)$$

Penetration depth λ can be considered as the depth at which the magnetic field penetrates into the superconductor and the magnetic field induction strength diminishes to 1/e of the strength at the surface. Which is expressed as: (for a weak magnetic field)

$$\lambda = \sqrt{\frac{mc^2\beta}{8\pi e^2|\alpha|}} \qquad (2.9)$$

Both coherence length ξ and penetration depth λ are temperature dependent.

When the temperature is close to Tc:

$$|\alpha| \propto (T_c - T) \qquad (2.10a)$$

Therefore:

$$\xi, \lambda \propto (T_c - T)^{-\frac{1}{2}} \qquad (2.10b)$$

2.2.3 High Temperature Superconductors

The BCS theory can describe the conductivity mechanism of ordinary superconductors well, however, it cannot explain high-temperature superconductors.

YBCO is quite similar to type II superconductors in that they both have Meissner states and intermediate states, but there are some differences in the intermediate states. As with type II superconductors, flux penetration can form an ordered lattice. However, in high temperature superconductors, when a sufficiently high magnetic field or temperature is applied, the lattices of the flux tubes begin to break up and move, which causes them to be able to interact with the current and so lose some energy. The measurement of electrical resistance is a measure of how much energy is lost in the passage of electrons through the material. The movement of the flux tubes causes the superconducting transition to expand to the superconducting state. So, the temperature transition in high temperature superconductors is not as sharp.

In classical superconductors, the moving charge is a Cooper pair consisting of two negatively charged electrons. However, for high temperature superconductors like YBCO, the Cooper pairs are deduced to be hole pairs [13]. It would be easier to investigate the motion of these holes compared to considering the collective motion of electrons. The carrier holes in copper-oxide superconductors come from the presence of Cu^{2+} and Cu^{3+} states. The ratio of these two states can be influenced by changing the oxygen content in the YBCO to affect the number of holes in the copper oxide conduction plane. So, changing the oxygen content in YBCO will change the critical temperature T_C [14].

There are two copper-oxygen planes in YBCO, the first one is the CuO_2 plane, which is above and below the yttrium atom, while the other plane is the CuO plane, which is near the yttrium atom, and the copper oxide plane is called the oxygen-deficient plane. The common feature of copper oxide superconductors is the presence of a copper oxide layer, and this also seems to be strongly related to the superconductivity of the system. The two planes of CuO_2 are separated by a yttrium atom. When superconducting currents pass through the two CuO_2 planes, the charge is transferred more easily between the ions in one layer than by hopping between two planes. Measurements in reference [13] actually show that the in-plane electrical current transport properties are superior.

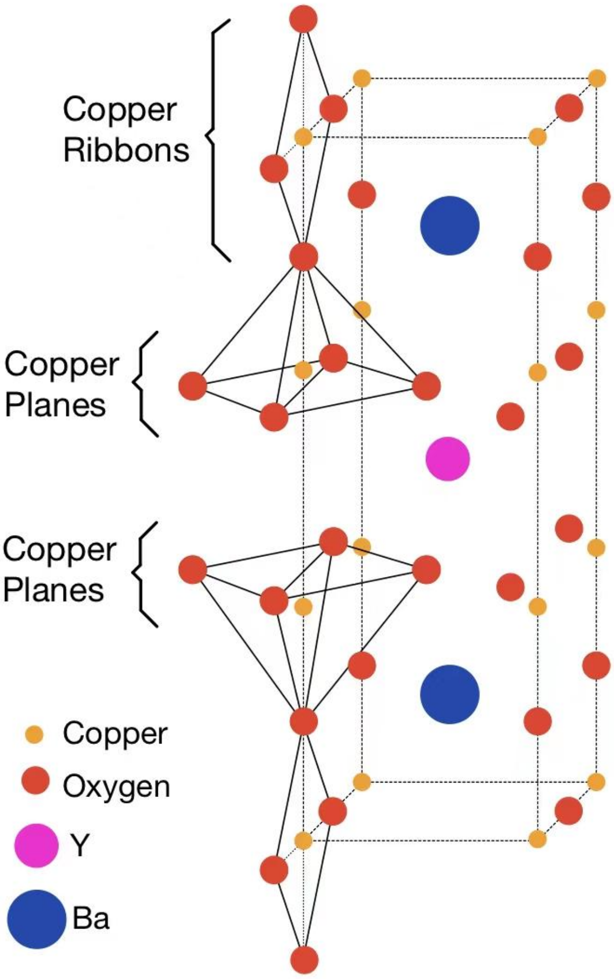

Figure 2.10: Schematic structure and chemical composition of YBCO.

2.3 Thin film growth

2.3.1 Molecular beam epitaxy

Molecular beam epitaxy (MBE) is a method to prepare single crystal film by "spraying" each component of the crystal and the desired doped atoms (molecules) from the effusion cells to the substrate in a certain ratio with a certain thermal movement speed under ultra-high vacuum conditions, similar to thermal evaporation.

The desired crystalline material is placed in the heated effusion cells in an ultra-high vacuum system. Effusion cells loaded with different components of crystalline materials are heated to different temperatures, resulting in evaporation, the molecular or atomic beams of material are subsequently deposited on the substrate, where a certain temperature is maintained. The heating temperature is determined by both the material type and the deposition rate.

The mean free path of the gas molecules of the evaporated material is much larger than the distance between the effusion cell and the substrate, so there is no collision with the residual gas molecules in the system before the molecular mass is deposited on the substrate and it becomes a well-oriented molecular beam. If several effusion cells are available in a single vacuum chamber, it is possible to make multi-semiconductor hybrid crystal heterostructures, and doping can be performed simultaneously. In our study, different materials Fe and Pd were heated to different temperatures in their respective effusion cells to produce molecular beams with different rates and deposited in a shuttered-deposition manner on a substrate at 25 degrees Celsius.

2.3.2 Deposition growth modes

The growth process of MBE epitaxial films has (i) atoms or molecules that are heated and ejected into the chamber in the form of a gas phase. (ii) These atoms or molecules are adsorbed on the substrate and form chemical bonds with substrate or attach via van der Waals forces. (iii) When heated, surface diffusion occurs in order to reach the minimum energy. (iv) When this energy barrier is overcome, nucleation and growth occurs, culminating in the ideal case in the formation of epitaxial thin films.

After the molecules have reached the substrate surface, there are different growth mechanisms in epitaxial growth, which were systematically classified by Ernst G. Bauer in 1958 into three main types: island growth mode (Volmer-Weber mode), layer by layer growth mode (Frank-van der Merwe mode) and island/layer growth mode (Stransky-Krastanov model). These are shown in figure 2.11.

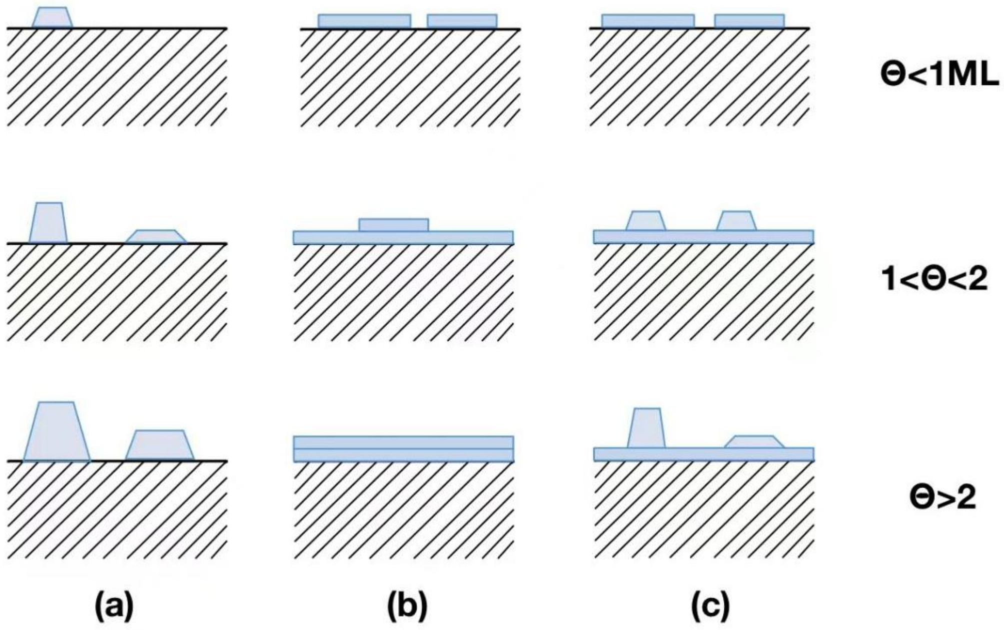

Figure 2.11: (a) island growth mode, (b) layer by layer growth mode, (c)island/layer growth mode, theta is coverage of the surface.

2.4 Proximity Effect

When a normal metal N and a superconductor S come in good contact with each other, the Cooper pairs from the superconductor can diffuse into the metal and "live" there for a period [8]. The penetration distance of Cooper pairs depends on the disorder of metal and temperature [10]. This phenomenon is known as the proximity effect.

2.3.1 Domain-wall superconductivity (DWS)

As shown in Figure 2.12, the superconducting thin film layer (S) is above and the ferromagnetic thin film layer (F) is below. The S layer is deposited on top of the F layer. Within the ferromagnetic film, the magnetic moment of the magnetic domain is along the Z-axis. At the beginning, the distribution of stray fields within the superconducting layer is almost uniform. Then, the temperature gradually decreases to T_c and superconductivity starts to appear in the superconducting layer, but not all superconducting currents are uniformly distributed within the entire superconducting surface, because Cooper pairs (CPs) preferentially nucleate within the low stray fields. In the absence of an applied electric field, CPs preferentially nucleate in the lowest stray field when the magnetic field in this region is less than the upper critical field H_{C2}. In the absence of an applied electric field, CPs forms when the magnetic field in this region is less than the upper critical field H_{C2}. As shown in the right panel in figure 2.12, superconductivity appears above the domain wall.

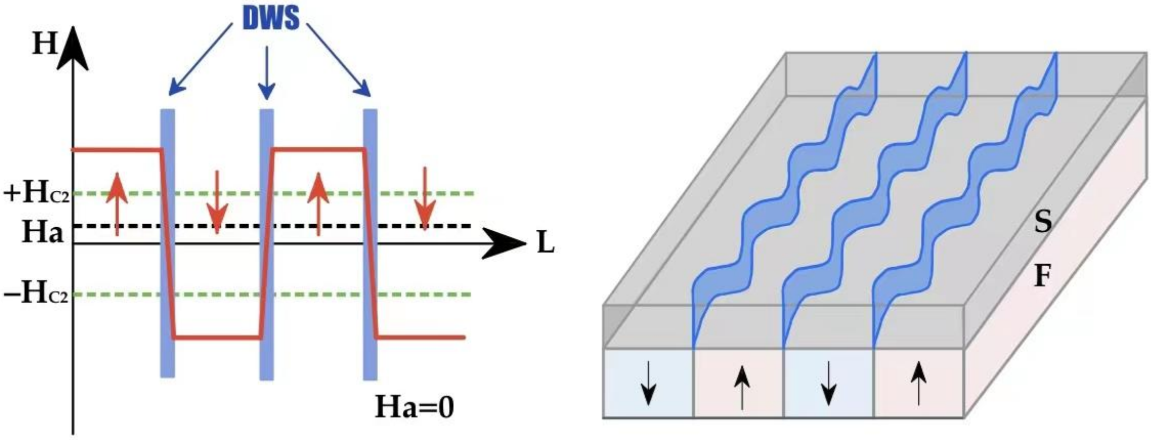

Figure.2.12: Schematic illustrations of domain-wall superconductivity (DWS) in superconductor/ferromagnet thin film system. The figure is adapted from [11].

2.3.2 Reverse-domain superconductivity (RDS)

As shown in Figure 2.13, when an applied magnetic field directed upward and perpendicular to the film is applied and the magnitude of the applied field is equal to the saturation field H_S, the stray field above the part of the domain, in which the direction of magnetic moment is opposite to the external magnetic field, becomes smaller than H_{C2}, i.e., the magnetic field above the reversed domain is fully compensated. In this case, the Cooper pair prefers to nucleate above the reversed domain, which is known as reverse-domain superconductivity [5].

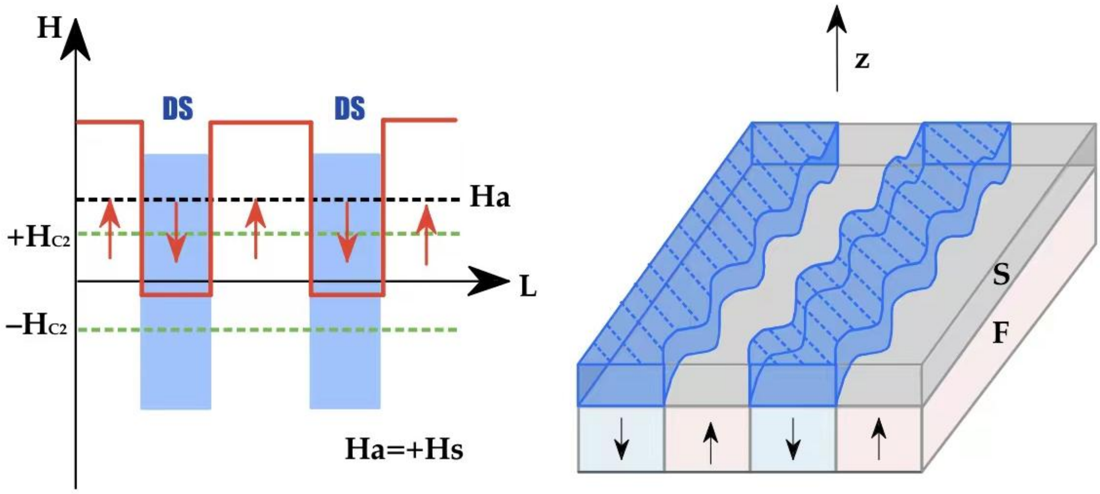

Figure 2.13: Schematic illustrations of reverse-domain superconductivity (RDS) in superconductor/ferromagnet thin film system. The figure is adapted from [11].

3 Experimental Methods

This chapter briefly describes the working and basic operating principles of the relevant experimental apparatus. The main focus of this study is on the growth of FePd thin film structures on the high temperature superconductor YBCO to form F/S heterostructured films. The growth environment is an oxide molecular beam epitaxy (OMBE) system. However, because Fe is sensitive to oxygen environment, there is no oxygen in these experiments in the OMBE. The main chamber is pumped out with a turbo/cryo pump combined with cryo shielding to a base pressure of $3\text{x}10^{-10}$ torr. Reflection high-energy electron diffraction (RHEED) can monitor the film growth pattern in real time during the growth of FePd films. The out-of-plane structure of the hybrid superconductor-ferromagnet (S/F) system was determined by X-Ray Diffraction. Finally, the magnetization field (M-H), resistance temperature (R-T) and resistance magnetic field (R-H) curves were measured through magnetic property measurement system (MPMS) and physical property measurement system (PPMS), respectively.

3.1 Sample Preparation

3.1.1 Oxide Molecular Beam Epitaxy

Molecular Beam Epitaxy is a high-precision technology for preparing single-crystal thin films, which is widely used in the semiconductor industry and has played a vital role in the spread of information technology. It enables the layer-by-layer growth of thin films on the atomic scale along the crystal axis direction of the substrate material under appropriate conditions. The advantages of this technique are: the growth rate of the film layer is slow, the precise control of the beam intensity can be realized, the layer components and doping concentrations can be adjusted rapidly in response to the changes from source.

As shown in Figure 3.1, the M600 OMBE system consists mainly of a load lock, a transfer line and a main deposition chamber.

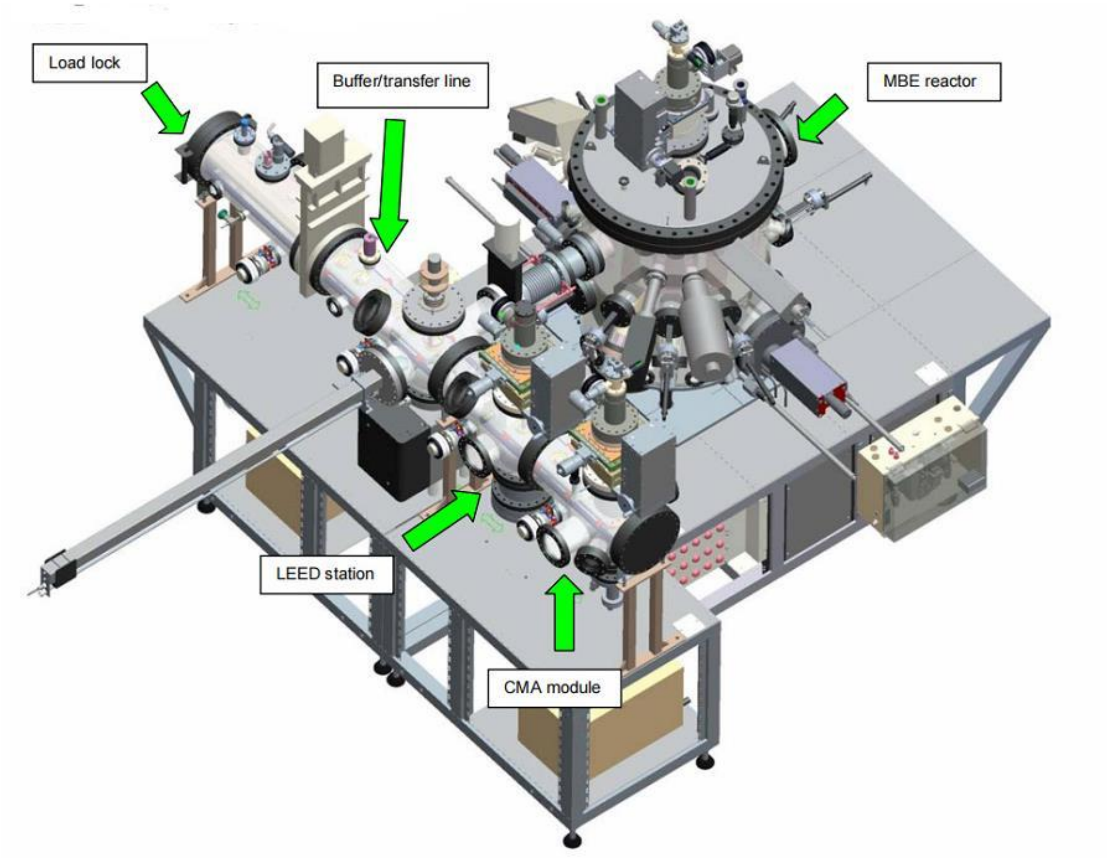

Figure 3.1: Layout of M600 MBE system.
This figure is taken from [15].

Sample introduction is as follows: After venting the load lock and putting on gloves, open the load lock and load the sample in a sample holder to the trolley. After closing the load lock door, the load lock space is pumped and when the pressure is almost equal to the pressure in the buffer line (within 4 decades), open the gate valve between the load lock and the buffer line. In the buffer line, the sample can be further transferred into the main growth chamber via the transfer arm.

As shown in figure 3.2, there are shutters above each effusion cell and the shutter switch allows flexible control of the deposition time of different components, thus enabling different growth modes (co-/ shuttered-deposition). A quartz crystal microbalance (QCB) provides real-time monitoring of the evaporation rate of individual components before deposition starts. Changing the temperature of the corresponding effusion cell regulates the evaporation rate of each component. Two effusion cells are used here, one containing (99.99%) Fe, and one with (99.99%) Pd.

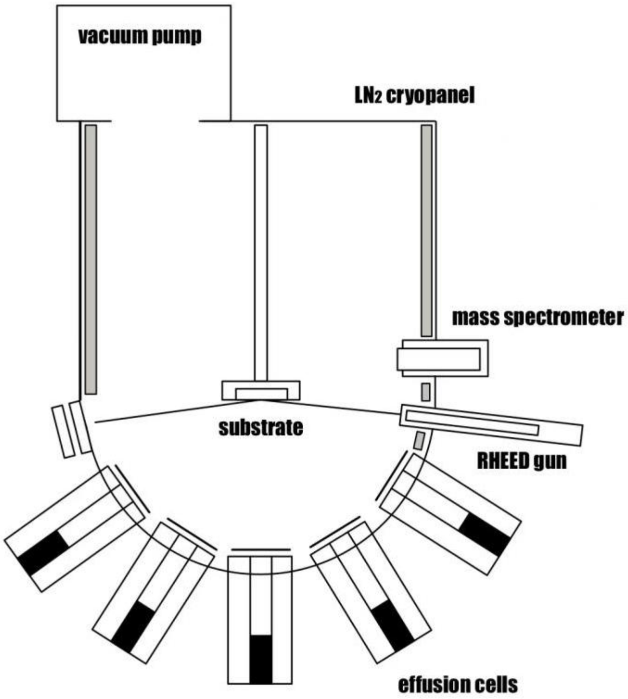

Figure 3.2: Schematic simplified cross section structure of the OMBE main chamber. This figure is adapted from [16].

3.1.2 Reflection High Energy Electron Diffraction RHEED

RHEED is an essential in-situ characterization technique for molecular beam epitaxy systems, where the penetration depth of the RHEED electron beam is only 1 - 2 atomic layers. Therefore the RHEED image shows the structural information of the sample surface at the atomic level. It allows diffraction investigations of the surface and growth monitoring during the film growth.

In this study, a RHEED system attached to the MBE device was used (figure 3.2). Different RHEED images can indicate that the samples have different surface structures, such as single crystalline (although further structural methods are needed, such as XRR/XRD to confirm crystallinity), polycrystalline, 3D island structures, etc. If the growth mode of the film is layer-by-layer, as shown in Figure 3.3 (b), the intensity versus time graph will show an oscillating curve when the intensity of the specular beam on the fluorescent screen is recorded. When the film surface is very flat, i.e., very low roughness, the corresponding beam intensity is the highest, i.e., 100% coverage. When the film surface is only 50% covered, when the surface roughness is the highest, the corresponding beam intensity is the lowest.

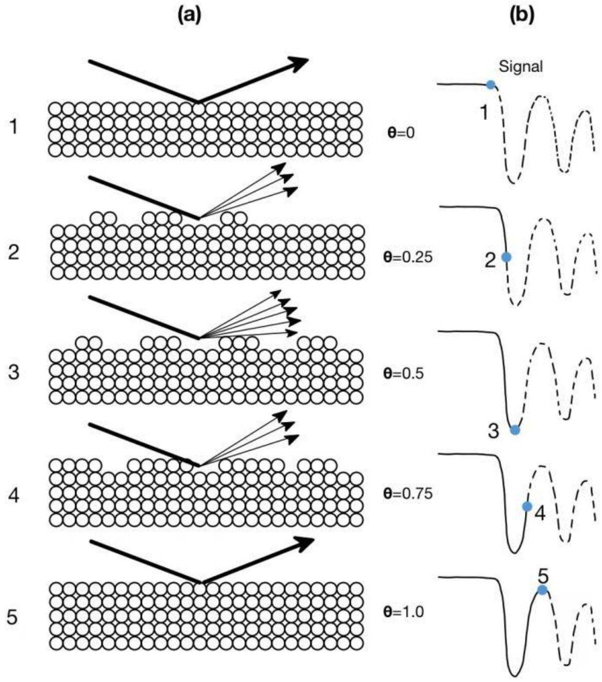

Figure 3.3: Model for RHEED intensity oscillations: (a) relationship between surface coverage and reflected electron beam; (b) beam intensity variation from RHEED screen. The figure is adapted from [17].

3.2 Characterization Methods

3.2.1 X-ray Diffractometer

As shown in Figure 3.4, the Bruker D8 Advance diffractometer instrument consists of an X-ray tube (left), the sample stage (middle) and the detector (right) and can be used to analyze the out-of-plane crystallinity. The system uses an X-ray source with a wavelength of 1.54055 Å, corresponding to the $\mathrm{Cu} - \mathrm{K}_{\alpha 1}$ transition. A highly collimated beam is achieved by two Göbel mirrors in front of and behind the sample. Monochromatic beam selection is achieved by mounting a channel-cut monochromator.

When X-rays are incident on the crystal surface, the crystal can act as a diffraction raster, so X-rays are scattered by different atoms in the crystal structure with different scattering waves, which interfere with each other to form a superposition of diffraction waves. Since the different intensities of diffraction waves are caused by the differences in crystal structure, diffraction patterns can indicate information about the crystal structure.

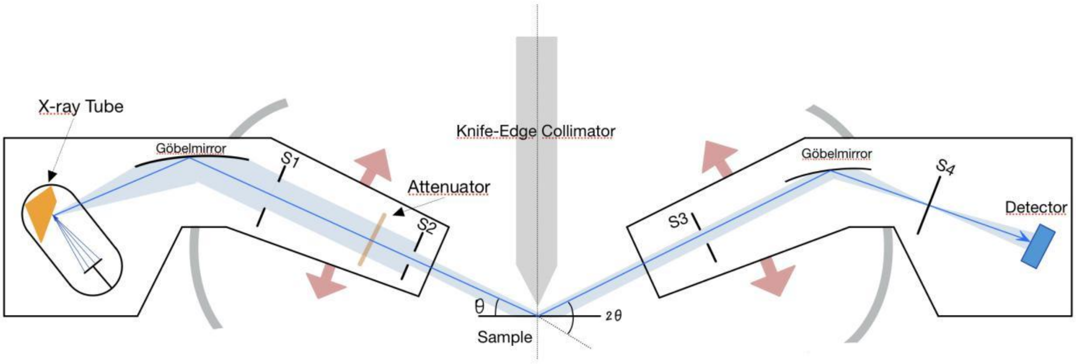

Figure 3.4: Schematic geometry of D8 X-ray Diffractometer.

3.2.2 Magnetic Property Measurement System

In this study, the magnetic properties of the samples were measured using the Magnetic Property Measurement System (MPMS) from Quantum Design Inc. (Fig.3.5). In the MPMS, the sample is mounted in a straw in a direction parallel or perpendicular to the magnetic field. It forms a second-order gradiometer together with a superconducting coil surrounding the outside. As the sample moves up and down through the coil, the local magnetic flux density varies with the motion of the sample.

The change in magnetic flux can be measured using a liquid helium-cooled SQUID (superconducting quantum interference device).

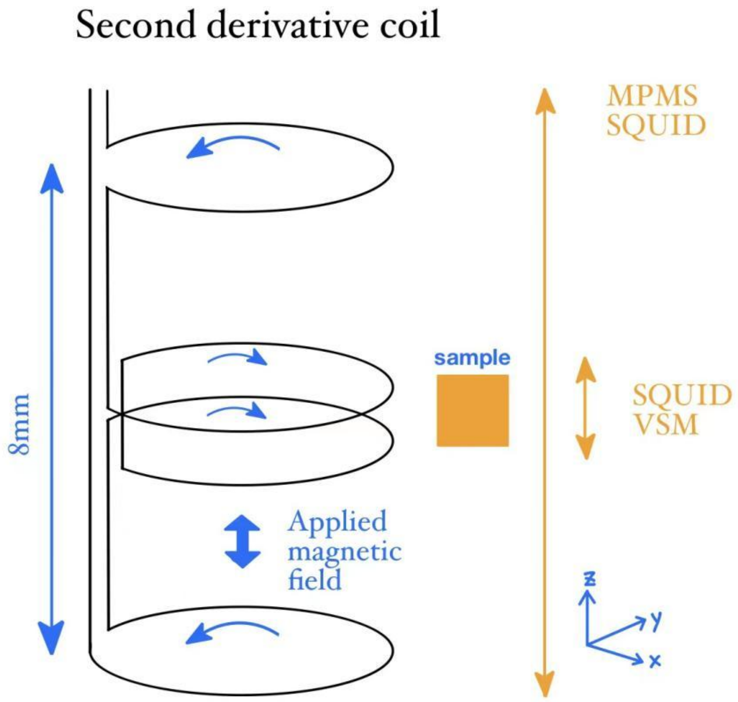

Figure 3.5: Schematic image of the principle of MPMS.

Using the Josephson effect, the SQUID can monitor very small changes in magnetic flux. Typically, SQUID is a superconductor ring, but it is interrupted by one or more Josephson junctions [18]. The voltage drop across the Josephson junctions changes as the externally varying magnetic flux is coupled to the Josephson loop. Combining the change in voltage with the motion of the sample determines the amount of flux coupled into the SQUID loop.

The samples were cut into small pieces of 4 mm×4 mm, and were fixed along the in-plane and out-of-plane directions using plastic pipettes and double-sided tape, then the change in magnetization was measured with the applied magnetic field, thus obtaining the hysteresis loops in different sample relevant directions

3.2.3 Physical Property Measurement System

The electrical transport properties of films are measured by the Quantum

Design Dynacool-PPMS (Physical Property Measurement System). The electrical transport properties of hybrid superconductor-ferromagnet (S/F) films at different temperatures and applied magnetic fields are measured by Quantum Design Dynacool-PPMS (Physical Property Measurement System). The working temperature range of PPMS is from 1.9K to 400 K and the applied magnetic field can be as high as 9 Tesla. The AC current used for these experiments is 10 μA.

A thermometer and a heater are installed below the sample puck for precise temperature control. A superconducting solenoid valve is mounted around the main chamber, which can generate the required magnetic field. The electrical transport properties can be measured by using silver wires and indium to realize connection between the corresponding contact points on the puck and sample .

As shown in Fig. 3.7, the sample is fixed to the rotatable sample holder with double-sided tape, followed by connecting the channel and the sample, ensuring that each wire is connected. Specific details of connecting the wires can be found in the Appendix. The sample rod is inserted vertically into the chamber of the PPMS, the chamber closed and evacuated. After coarse measurement of the resistance and ensuring that the sample is mounted correctly, the temperature is lowered to near T_C and the resistance versus temperature curves are measured to determine T_C, followed by the curve of resistance versus the applied magnetic field.

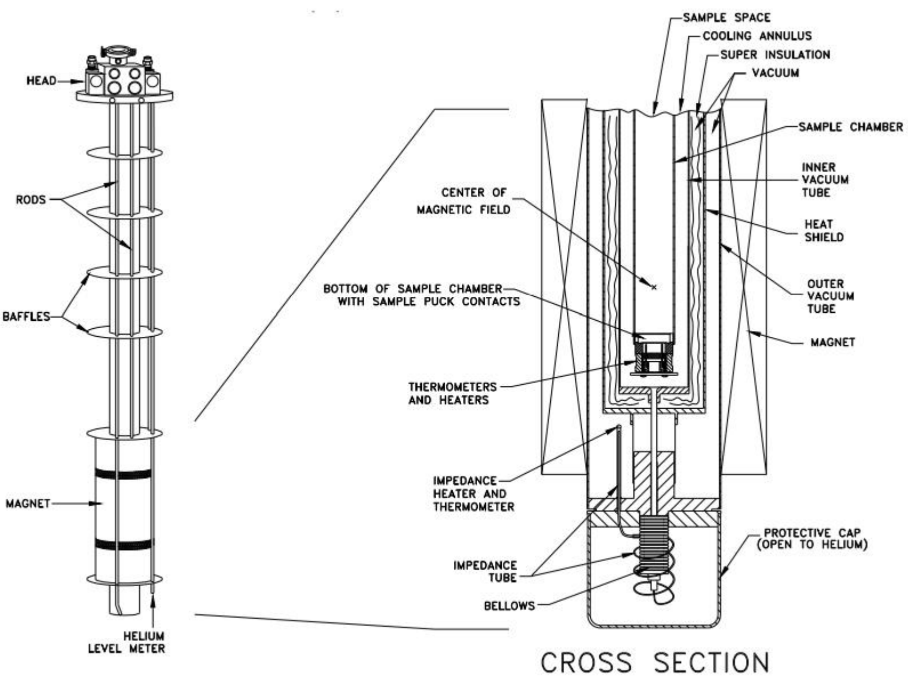

Figure 3.6: Schematic image of major components of the PPMS. Figure is taken from [33].

Figure 3.7: Schematic image of the rotater sample holder in PPMS.

4 Sample preparation

The heterostructure prepared in this study was $YBa_2Cu_3O_{7-x}$/FePd (HTS/F). Prof. Dr. Michael Faley used high oxygen pressure sputtering (HOPS) to prepare YBCO films with a transition temperature of about 90K at the ER-C-1 Forschungszentrum Jülich, while the main preparation task in this study was to grow FePd ferromagnetic films on YBCO superconducting layer using MBE. The details of the preparation are given in the subsequent part of this chapter.

4.1.1 YBCO

The substrate MgO from CrysTec GmbH is one-side polished with lattice constant a=0.4212nm [21]. During the YBCO thin film deposition, the substrate is placed on a heater and the substrate temperature is around 800℃ in atmosphere of pure (99.999%) oxygen at a pressure of about 3 mbar [22].

The recipe for YBCO deposition on MgO developed is as follows: Before depositing YBCO on magnesium oxide, two buffer layers are deposited: the first one is a YBCO seed layer. MgO has a rocksalt structure, therefore, a thin film with a perovskite structure is needed to be deposited above that, so first 3 nm of YBCO is deposited on ion beam etched and textured MgO as a graphoepitaxial seed layer. Subsequently an epitaxial $SrTiO_3$ (STO) blocking buffer layer of 20 nm thickness is deposited, which allows a good c-axis oriented epitaxial growth of the subsequent superconducting YBCO film sputtered above it and also blocks diffusion of impurities from MgO substrate. In addition, the hygroscopic surface of the MgO substrate is kept from degrading in air or during a lithography process [22].

4.1.2 Growth parameters

The film thicknesses and deposition rates for experiments were obtained from the optimized experimental data of Annika Stellhorn [20] and Prof. Dr. Michael Faley [22].

In this study, a total of four different samples of film were prepared, as shown in the table 4.1 below. The pure YBCO and sample MgO/FePd is the comparison group while the F/S group is based on my project thesis study [23] using the sample grown with shuttered deposition at room temperature.

sample	Brief condition	substrate	deposition method	deposition temperature	Thickness /nm
0685	Optimized YBCO/FePd	MgO-YBCO	shuttered	RT	20
0708	Fresh YBCO/FePd	MgO-YBCO	shuttered	RT	40
0829	Pure YBCO	MgO	HOPS	800℃	60
0679	MgO/FePd	MgO	shuttered	RT	40

Table 4.1 Sample list of comparison group and F/S system group

Although OMBE is used in the deposition of FePd, there is no oxygen in the deposition process. In fact, oxygen is detrimental to the FePd deposition as it oxidizes the iron in FePd. This is balanced with the fact that YBCO will lose oxygen in the oxygen-free environment leading to a change of T_C.

After the deposition of YBCO, each sample was transferred immediately to the MBE main chamber for FePd deposition. For the sample 0685, the optimization refers to the further increase of the transition temperature Tc of the YBCO sample to 90.1 K. In addition, the FePd layer in this sample is only 20 nm, which is to enable the TEM experiments to be performed more easily.

In order to grow single-crystal films with high perpendicular magnetic anisotropy with suitable stoichiometric ratios, the growth rates of Fe and Pd were directly adopted from the optimal parameters in Annika Stellhorn's paper [20]. By varying the temperature of the effusion cells, the evaporation rate of the individual materials can be changed:

$$T = Ct\frac{\partial f}{\partial t} \qquad (4.1)$$

where T is the thin film thickness, C is a constant, t is the growth time and $\partial f / \partial t$ is the change rate of the resonant frequency.

4.1.3 Thin Film Growth

For the MgO/FePd sample in the comparison group, a Pd buffer layer was first deposited on the annealed smooth MgO substrate with the aim of solving the problem of large differences in lattice mismatch. The existence of the Pd buffer layer reduced the lattice mismatch from 8.59% to 1.03%. The epitaxial Pd buffer layer was then annealed in 350℃ for 30 min with the aim of obtaining a uniform and flat surface. Subsequently, FePd films were deposited using shuttered-deposition growth method. A final Pd capping layer was deposited to prevent FePd oxidation.

For the pure YBCO samples in the comparison group, the specific deposition parameters have been described in section 4.1.1.

The specific growth schema was shown in my project thesis [23]. Specific details of the FePd growth parameters can be found in Table 4.2 below.

sample	**Brief conditions**	t_{Pd} [s]	$-\partial f / \partial t_{Pd}$ [Hz/s]	t_{Fe} [s]	$-\partial f / \partial t_{Fe}$ [Hz/s]
0679	MgO/FePd (sh, RT)	2310	-0.914	2090	-0.494
0685	Optimized YBCO/FePd (sh, RT)	1155	-0.915	1045	-0.493
0708	New YBCO/FePd (sh, RT)	2310	-0.923	2090	-0.494

Table 4.2 Optimized growth parameters used for co-deposition and shuttered growth.

For the F/S system group, the YBCO thin film was deposited using HOPS as described in Sec. 4.1.1. and then it was first quickly (within 2 min.) transferred from the sputtering chamber to the MBE main chamber. On the “YBCO substrate”, we directly started depositing FePd in shuttered -deposition method, by opening and closing the shutter continuously, thus achieving interleaved deposition of Fe and Pd. Finally, a Pd capping layer

(2nm) was deposited to prevent FePd oxidation. Only the shuttered-deposition mode was chosen here because, based on the previous study, if a high PMA film needs to be grown, co-deposition and increasing the growth temperature of substrate to 230℃ is required, but in a high vacuum MBE chamber, the high temperature will lead to loss of oxygen from the YBCO film. Once the oxygen content in YBCO changes, it will have a great impact on the T_C or the superconductivity of YBCO.

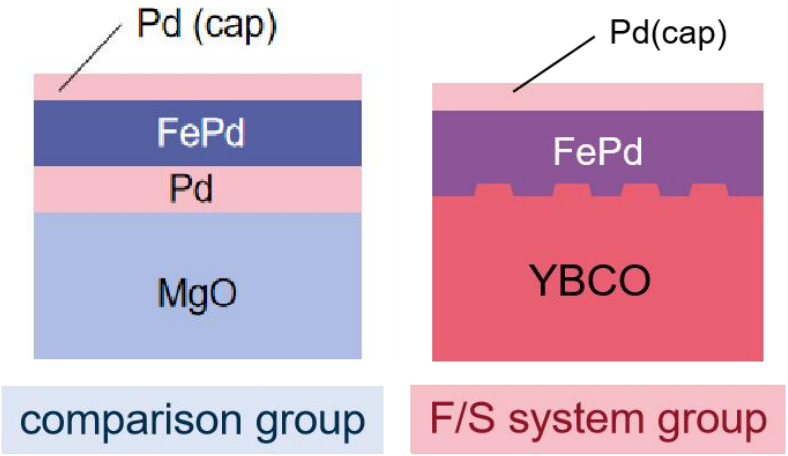

Figure 4.1: Schematic structure of F group and F/S system group.

4.1.4 Reflection High-Energy Electron Diffraction

In Reflection High Energy Electron Diffraction (RHEED), an electron beam with a defined energy is emitted from the electron gun at a small angle (usually 1 - 2° of grazing angle) to the sample surface, which results in a small momentum perpendicular to the sample surface. At the same time, the electrons are scattered by the Coulomb field, so the penetration depth of the electron beam is only 1- 2 atomic layers. RHEED reflects the structural information of the sample surface, and therefore plays a great role in the study of crystal growth and surface defects [28]. For the multilayer thin film system in this study, in-situ RHEED can monitor the growth pattern of each layer in real time during the growth of the film, and also give us a qualitative check on the surface roughness and surface reconstruction.

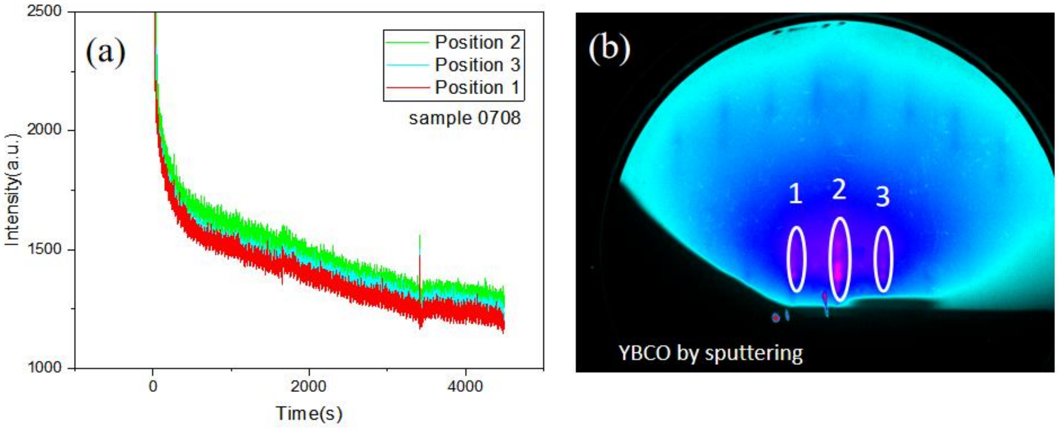

Figure 4.2: RHEED patterns of YBCO made by HOPS.

Figure 4.2 shows the intensity change of three RHEED spots for the sample “new YBCO/FePd (sh, RT) ” during the FePd deposition. The circled parts in the right panel of Figure 4.2 correspond to the three curves in the left panel, respectively. It is obvious from the right panel that the YBCO prepared by sputtering is epitaxially grown, but the innate spiral structure leads to a relatively high surface roughness of the YBCO, so the stripe pattern in the RHEED image is also relatively blurred without Kikuchi lines. Each curve in the left image has a slight fluctuation, but this does not correspond to layer by layer growth, but to the opening and closing of the shutter. The RHEED pattern for layer-by-layer growth mode is shown in the literature [24], where it fluctuates relatively more slowly and the peaks and valleys are farther apart, provided the deposition parameters are almost identical.

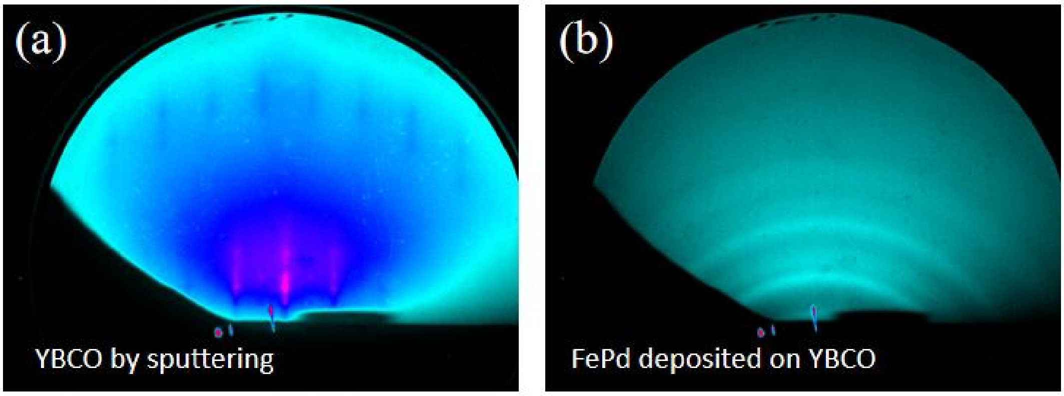

Figure 4.3: the RHEED patterns before and after the growth of FePd.

After starting FePd deposition, as shown in Fig.4.3 (b), the ring pattern is shown as soon as the shutter above Pd is opened. The circular pattern can be interpreted as a continuous distribution of the intensity of the Debye ring along its circumference [25]. This indicates that the FePd particles have a random orientation when FePd deposited on YBCO. Therefore, we infer that the deposited FePd is polycrystalline. Unfortunately, due to fact that the loss of oxygen in YBCO impairs its superconducting properties, we cannot anneal the YBCO film in the vacuum of the MBE chamber to improve the FePd structure, as this would also lead to deoxygenation of the YBCO, and destroy it's superconducting properties. The fact that the RHEED image shows this ring pattern means there is a lack of sufficient energy for the deposited Pd and Fe atoms, and they therefore have relatively low mobility, leading to a polycrystalline formation of FePd, despite the good lattice matching of 1.03% between YBCO and FePd.

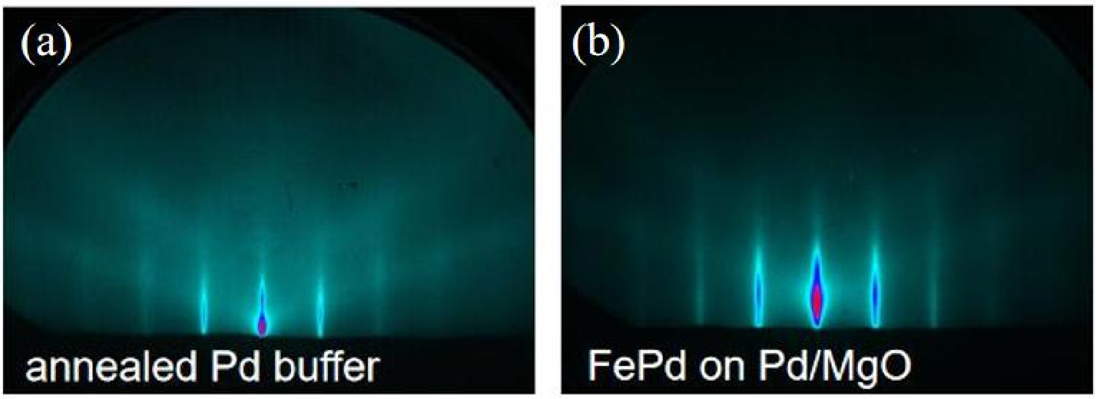

Figure 4.4: FePd deposited on annealed MgO/Pd (substrate/buffer layer).

For the comparison group shown in Fig.4.4, FePd deposited at room temperature on annealed smooth MgO/Pd had a very smooth surface and good epitaxial growth, as concluded from the clear Kikuchi lines and modulated stripe patterns in the RHEED images.

5 Results and Discussion

5.1 X-ray characterization

The X-ray diffraction spectra of crystalline substances with different elements or different structures will show differences in the number of diffraction peaks, angular position, relative intensity and diffraction peak shape (based on the Bragg equation). By comparing with standard spectra, it is possible to know which phases the measured sample consists of.

The measurements were performed on the D-8 diffractometer of JCNS-2, except for the curve in red of "pure YBCO sample 0829", which was obtained on the XRD instrument of PGI-7. The diffraction vector is always perpendicular to the surface of the sample; thus all the measured parameters are out-of-plane lattice constants.

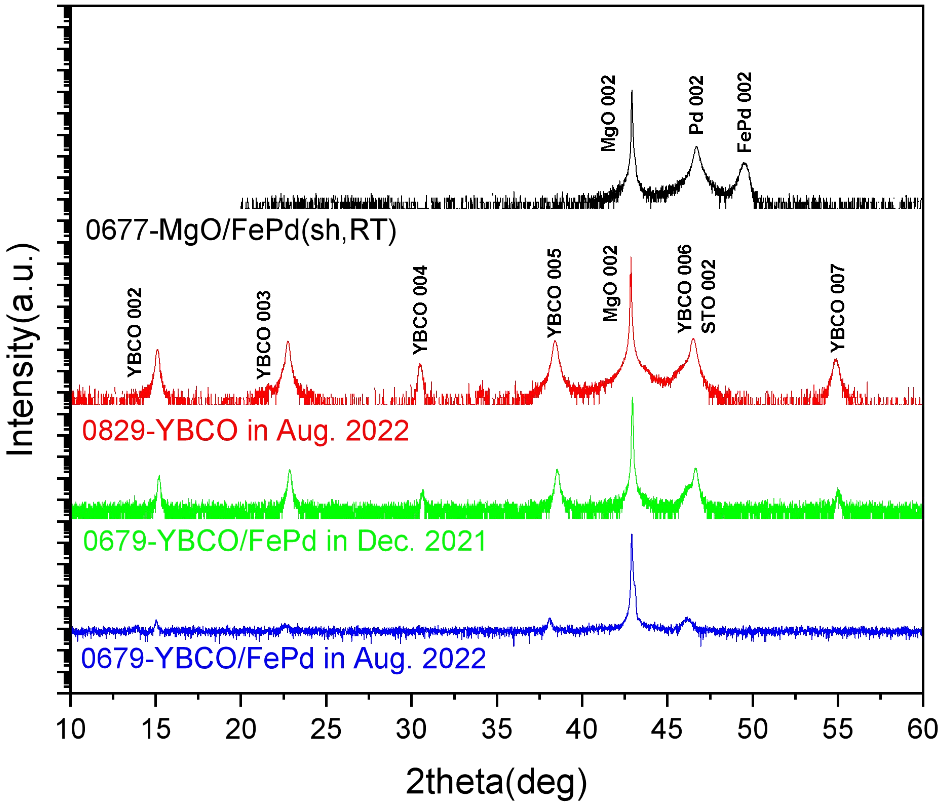

Figure 5.1: X-ray diffraction spectra of comparison group and F/S group. Comparison group: "0677-FePd" sample in black line, "0829-pure YBCO" in red line. F/S group: the same sample " 0679-YBCO/FePd". The green line was measured immediately after sample preparation in Dec. 2021, and the blue line was measured again after the samples were stored in the vacuum chamber for 8 months.

For the FePd sample “0677” in comparison group, the XRD patterns are shown in figure 5.1 as the black line. The positions of the FePd (002) and MgO (002) peaks were determined to be 42.95 and 46.66 degrees, respectively. The red line is the “pure YBCO sample 0829” measured in PGI-7 and the positions of all YBCO peaks can be clearly marked as in the YBCO curves calibrated in the literature [29], they will be used as a comparison group. The green line is YBCO/FePd (sh, RT) sample 0679. It can be seen that the peaks of the YBCO in green and the peaks of pure YBCO in red almost coincide, only the intensity of the peaks is slightly lower, but this may be due to the use of the different diffractometer (for sample 0829) of PGI-7 as mentioned before. However, compared to the black line of sample 0677, the FePd peak disappears. This corresponds exactly to the conclusion of polycrystalline FePd that shows up in the RHEED pattern as a powder ring. The last blue curve corresponds to the sample 0679, but there was a eight-month gap between the XRD measurement and the sample preparation. During this time, the sample underwent many measurements and was then stored in a vacuum chamber, but the blue curve shows severe YBCO degradation. There are two reasons for this: one is that YBCO itself is very sensitive to air, so a lot of contact with air occurred during the process of placing and removing the samples while doing the experiments. Secondly, when doing the R-T curve measurement, because the temperature needs to be decreased to 80K during the experiment, when the measurement is over and the sample is taken out directly after warming up to room temperature. Although the chamber of PPMS was warmed up to room temperature, both the sample and the sample holder did not really return to room temperature due to the different thermal conductivity, so water condensate was formed during the removal process and attached to the sample, which led to serious degradation of the sample. Further details about degradation of YBCO is given in the appendix 7.2.

5.2 Magnetoresistance with in- and out-of-plane magnetic field

5.2.1 sample 0685-optimized YBCO/FePd

Due to the high sensitivity of YBCO to air, the samples were cut into three pieces for simultaneous measurements in the R-T, R-H in-plane and out-of-plane directions in order to ensure consistent exposure times of YBCO to air.

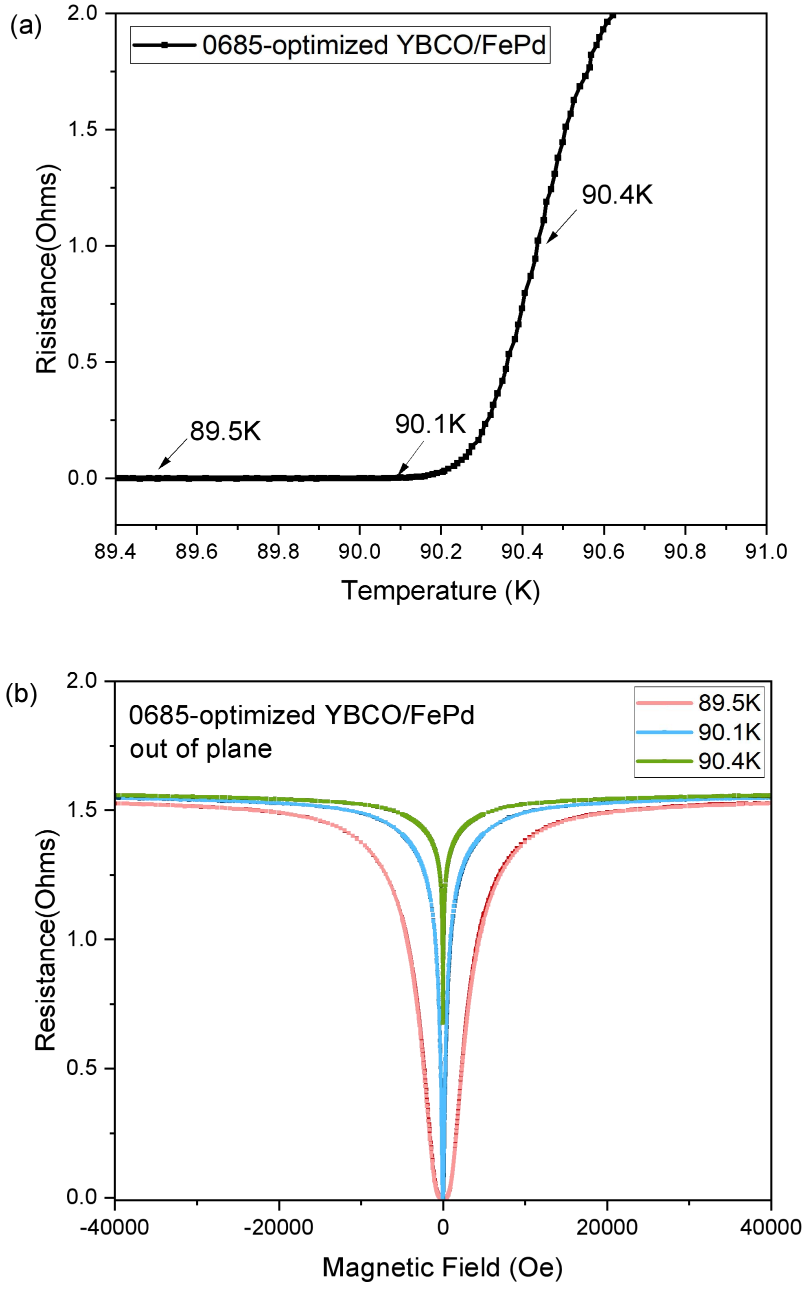

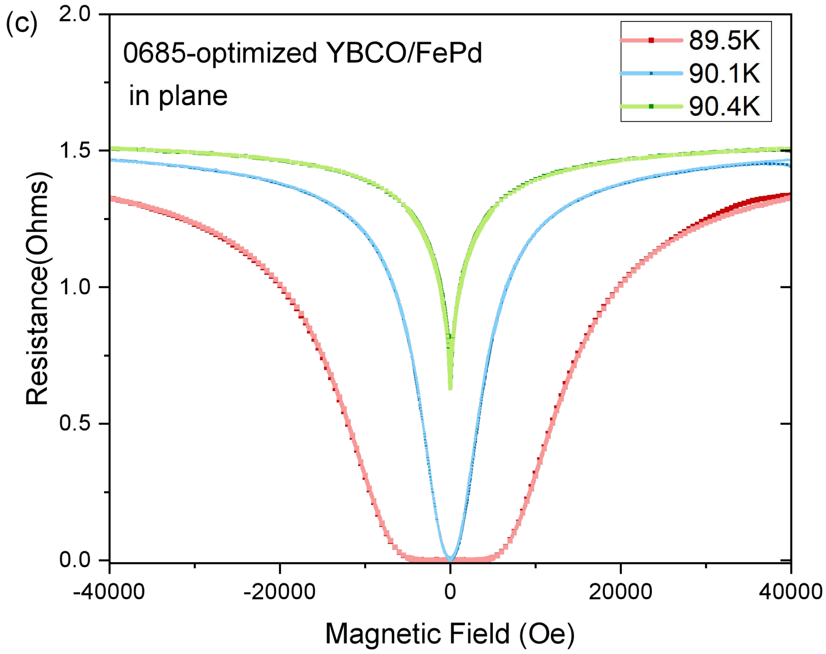

Figure 5.2: (a) Resistance vs. Temperature and (b) Magnetic Field curves of sample 0685 in both out-of-and (c) in-plane direction.

As shown in Fig.5.2(a), the optimized sample 0685 was first subjected to the determination of the transition temperature T_C as well as the rough measurement of the resistance variation with the applied magnetic field. The optimized sample 0685 has a high transition temperature of 90.1 K, which is closely related to the oxygen content in YBCO. The three temperatures marked with arrows (89.5K, 90.1K, 90.4K) are the experimental temperatures used in the subsequent measurement of the R-H curve.

In both the in- and out-of-plane directions of the R-H curve, a higher resistance with increasing external magnetic field is observed. This is due to the fact that electrons collide with the nucleus under the influence of an external magnetic field, thus causing an increase in resistance. This also indicates that applied external field destroys superconductivity behavior and the superconducting state at lower temperatures requires a higher magnetic field to break down. One can combine figure 2.8(b) with figure 5.2(c), in the in-plane direction, when the temperature is 89.5 K, H_{C2} is about 5 kOe. while the temperature rises to 90.1 K (T_C), H_{C2} becomes about 0 Oe. It is clear that H_{C2} decreases with increasing temperature.

5.2.2 Fresh sample 0708-New YBCO/FePd

Since the optimized sample 0685 had been cut into three pieces and the

R-H experiment had been performed in PPMS for two weeks, re-measurement of the R-T curve of the optimized sample 0685 was performed and the transition temperature had changed from 90.1K to 89.6K after 3 months. A fresh sample 0708 was prepared.

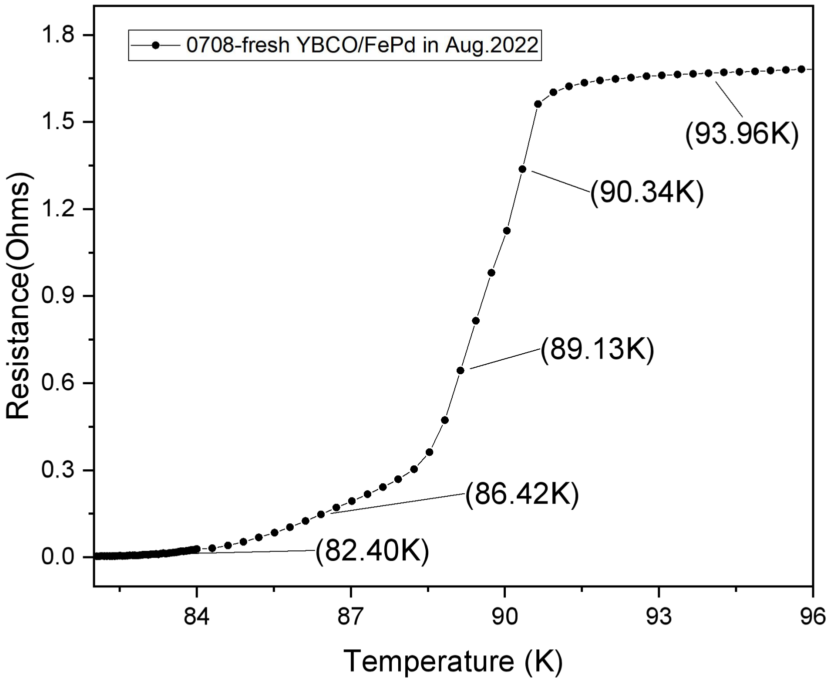

Figure 5.3: Resistance vs. Temperature curve of sample 0708 was measured in Aug. 2022.

The transition temperature of the sample 0708 is only 83.3 K as shown in Figure 5.3, but this time the R-H curve was measured in a finer interval [-4000Oe, +4000Oe] to get more detailed information. We speculated that the depression of T_C and the change of the shape of the curve, this time, could be due to proximity effects.

In the R-H curve measurement (out-of-plane) shown in figure 5.4, the temperature was first decreased to 82K (T_C=83.3K). At first, the applied magnetic field changed from 4000Oe to -4000Oe at a rate of 5 Oe/min to obtain the dark-colored curve on the right in figure 5.4 and then the applied magnetic field changed from -4000Oe to 4000Oe to obtain the light-colored curve. Arrows indicate direction of magnetic field sweep. The rate of change of the applied magnetic field was 0.01Oe/min in the interval of ±200Oe. The temperature was increased to 83 K, 85 K, 87 K and 89 K and the above procedure was repeated in turn to obtain the R-H curves at different temperatures. In the out-of-plane direction the resistance still decreases as the applied magnetic field decreases, however, when the applied magnetic field changes from positive to negative, the minimum of the curve (dip) appears in the positive magnetic field region (15.44 Oe) as shown in the dark-colored curve.

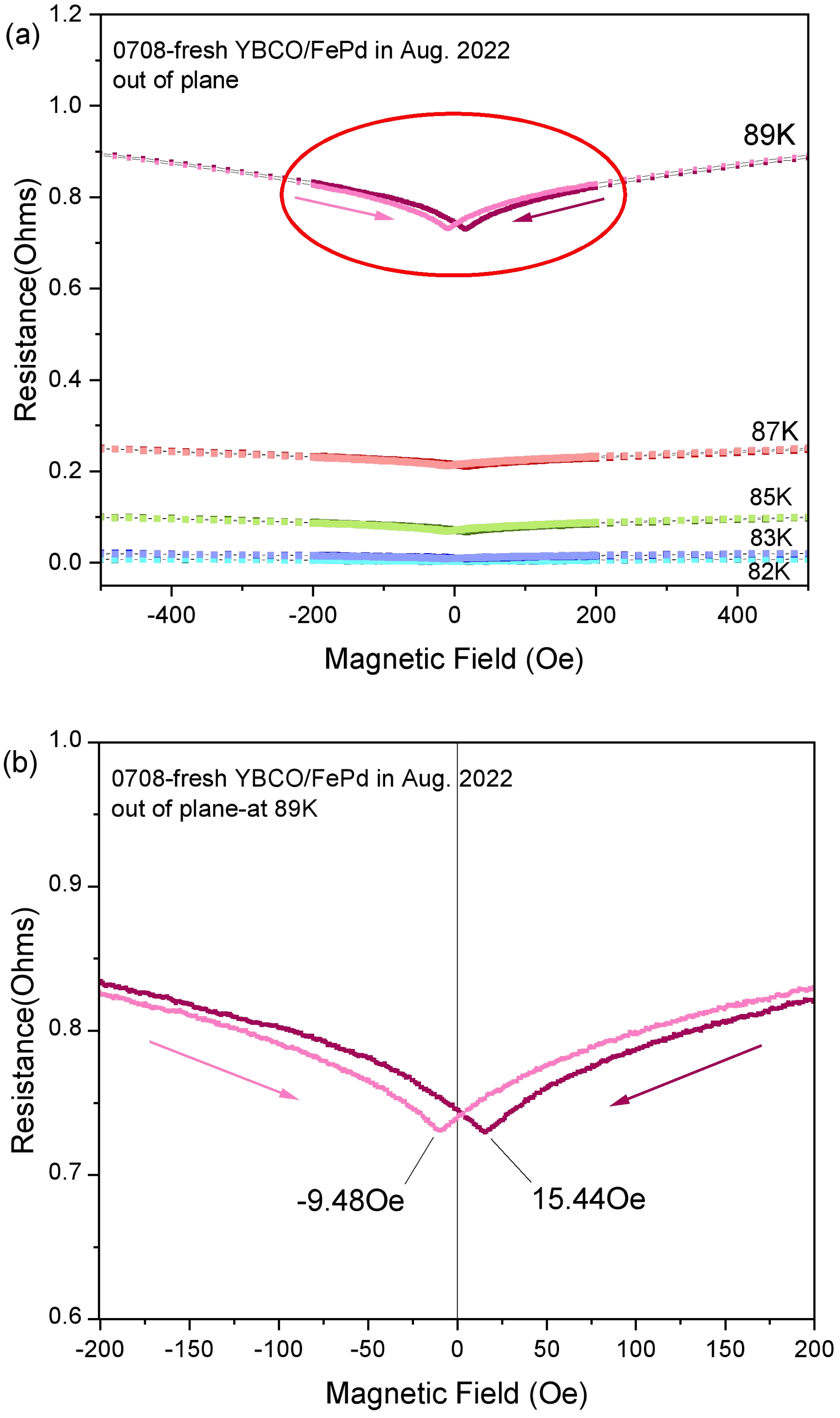

Figure 5.4: (a) Detailed R-H curves of sample 0708 in out-of-plane

direction. The measurement was performed in Aug. 2022. Figure 5.4(b) shows an enlarged detail of the red circled part of Figure 5.4(a).

In PPMS, the direction of the magnetic field is perpendicular to the ground and it can not be changed. But the direction of the sample can be changed by fixing the sample on the rotater sample holder. For example, if we turn the sample from out-of-plane direction to in-plane direction, just set the angle from 0 degrees to 90 degrees, the rotater will make the sample turn from parallel to the ground direction (out-of-plane) to perpendicular to the ground direction (in-plane). The out-of-plane direction means that the sample is parallel to the ground, and since the direction of the applied magnetic field inside the PPMS is always perpendicular to the ground, it means that the flat edge of the substrate is perpendicular to the direction of the applied magnetic field at this time.

The procedure of in-plane direction R-H measurements are nearly the same as the out-of-plane direction R-H experiments, except that the applied magnetic field direction is parallel to the flat edge of substrate. In the in-plane direction there is a completely different trend as below:

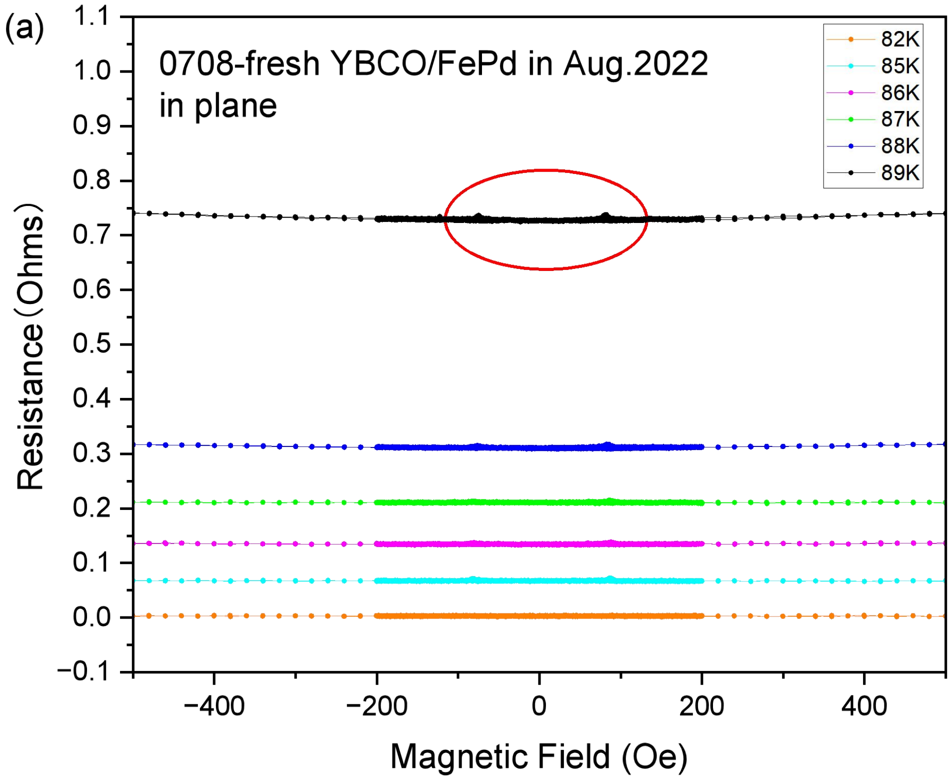

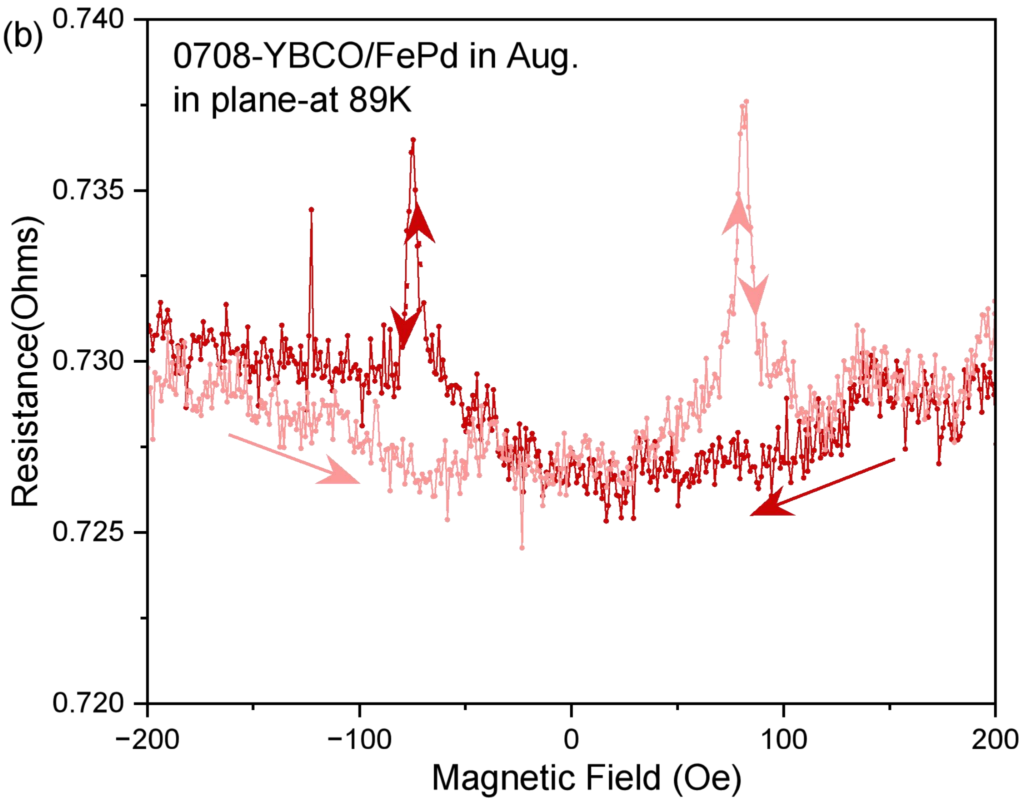

Figure 5.5: Detailed R-H curves of sample 0708 in in-plane direction. The measurement was performed on August 22. Figure 5.5(b) shows an enlarged detail of the red circled part of Figure 5.5(a).

In Figure. 5.5 (a), the upward peaks in the resistance appeared when the temperature increased from 82K to 85K (T_C=83.3K) in the in-plane direction. As shown in the dark red curve in figure.5.5 (b), when the applied magnetic field changes from positive to negative, there is a sudden upward peak in the negative resistance region at about -80 Oe.

5.2.3 Re-measurement for sample 0708

Since the temperature interval set for the R-H curve measured in August did not allow the trend of the upward peaks to be seen, a second set of R-H experiments was performed a month later (in Sep. 2022) for the same sample 0708 with a smaller temperature gradient range as shown in Fig.5.6. in order to observe the detailed change and trend of the sudden upward peak in resistance more clearly. Since T_C varies with the oxygen content in YBCO, i.e. the sample has a high sensitivity to air, the R-T curve must be performed before each measurement of the R-H curve in order to estimate the state of the YBCO, and find the region of interest around T_C. The R-H curve corresponding to the R-T curve in Fig. 5.6 is shown in Fig. 5.7.

For the reasons mentioned in section 4.2: the sample is contaminated with condensate water during removal from the PPMS. Sample 0708 likewise loses part of its superconductivity as shown in Fig. 5.7, which leads to the fact that even when the temperature is lowered to 86 K, the sample still has a small resistance value of about 1.5 ohms.

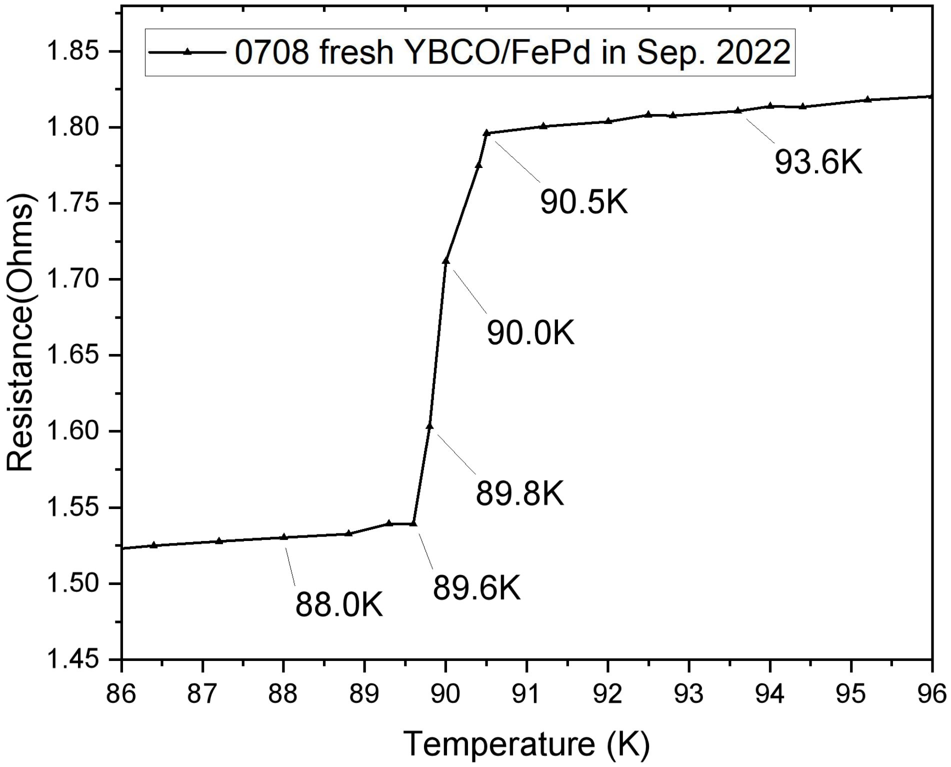

Figure 5.6: Remeasured R-T curves of sample 0708 (made in Aug. 2022) were measured in Sep. 2022.

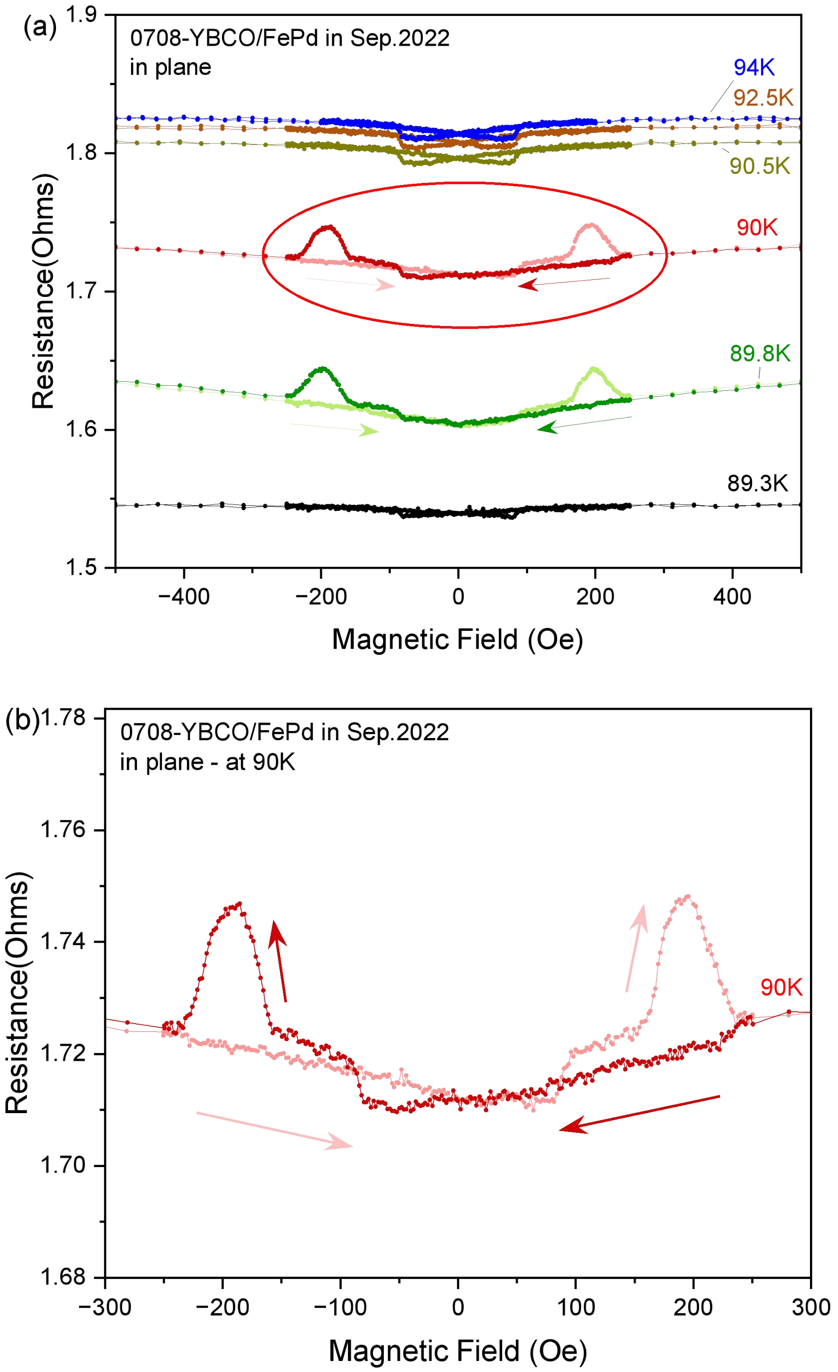

Figure 5.7: Remeasured detailed R-H curves of sample 0708 in Sep. 27. (b) shows an enlarged detail of the red circled part of (a).

However, the R-H curve of the sample mainly observes the trend of resistance with the applied magnetic field, so it still shows a sudden change in resistance, indicating at least part of the film remained superconducting. As shown in figure 5.7 (a), when the temperature rises from 89.3 K to 89.8K the upward peaks appear and they disappear when the temperature rises from 90K to 90.5 K. Referring to the R-T curve measured in Sep. in figure.5.6, it is not difficult to speculate that upward peaks will only appear in the superconducting temperature transition region. In the transition interval, the upward peaks at 90K and 89.3 K occur at ±197 Oe and ±190 Oe, respectively.

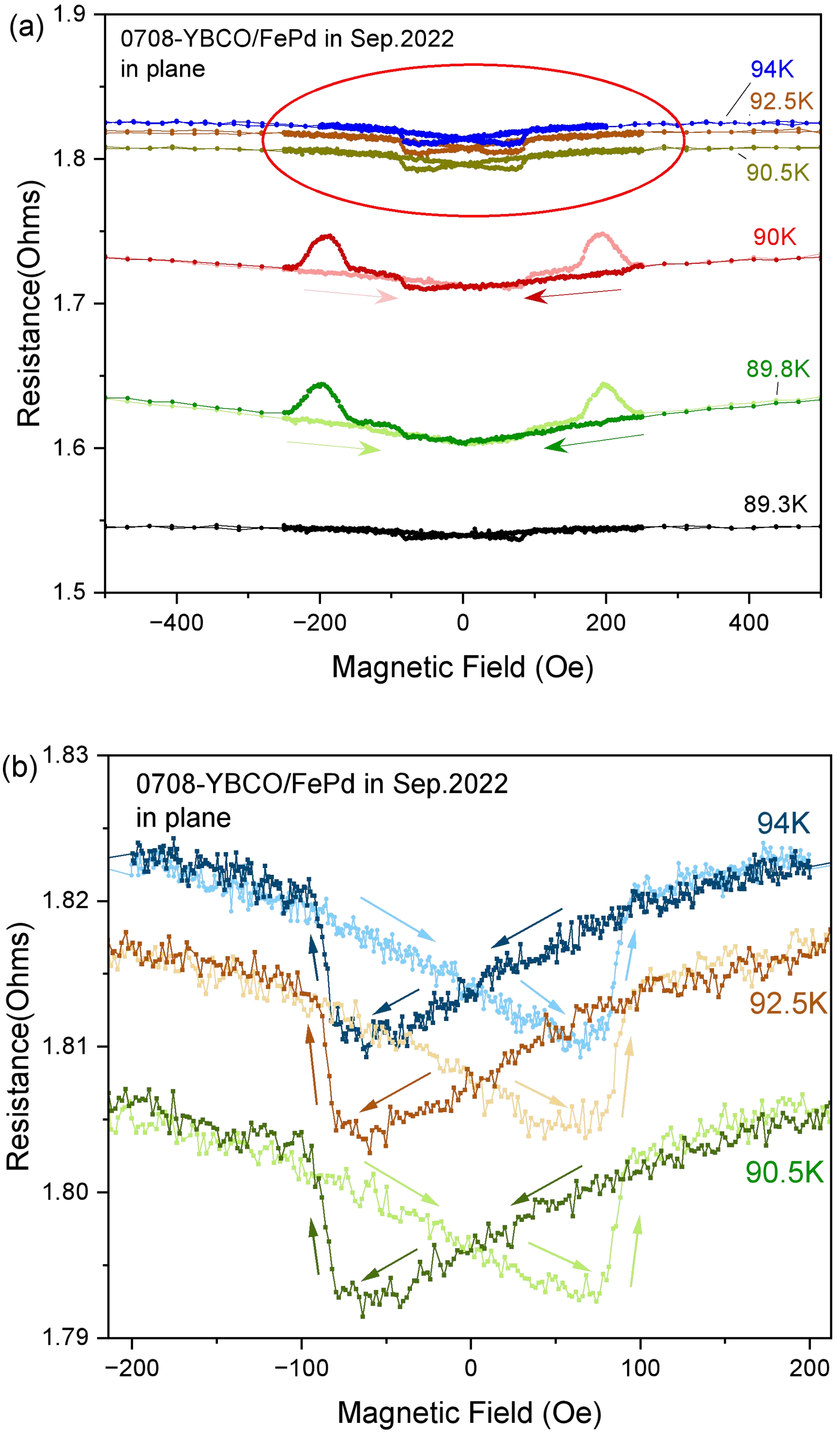

Figure 5.8: Remeasured detailed R-H curves of sample 0708 above the transition temperature interval. (b) shows an enlarged detail of the red circled part of (a).

In the interval above 90.5 K and below 89.3 K, there is a clear downward dip in R-H as the applied magnetic field changes from positive to negative as shown in figure 5.8 (b) in the dark-colored blue curve and the minimum is at about -74 Oe. This dip is also present on the transition interval, although it is not as distinct as in the high and low temperature regions.

5.3 Magnetic properties in both in- and out-of-plane direction

In order to observe the change of the coercive field with temperature for the F/S group samples, M-H experiments were measured at different temperatures. The M-H curves were obtained by MPMS measurements and the different orientations were achieved by placing the samples in different plastic straws perpendicular or parallel to the external magnetic field.

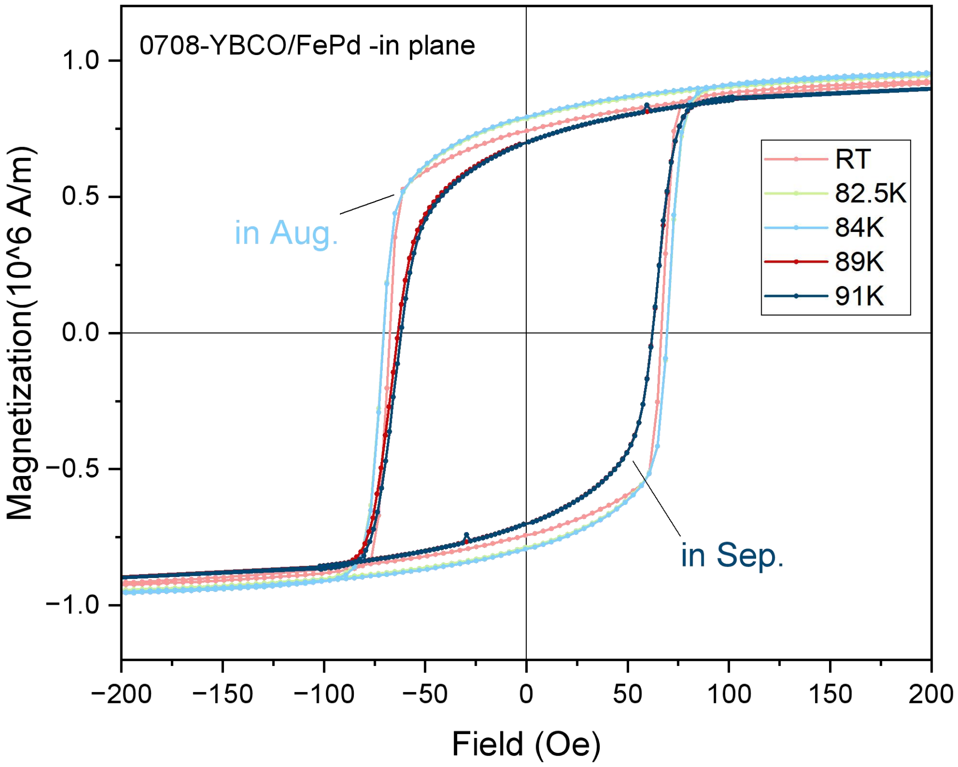

Figure 5.9: M-H curve of sample 0708 at different temperatures in in-plane direction (light-colored curves were measured in Aug., dark-colored curves were measured in Sep.).

In the in-plane M-H curves of Figure 5.9, the light-colored curves were measured in August, while the dark-colored curve was measured in September.

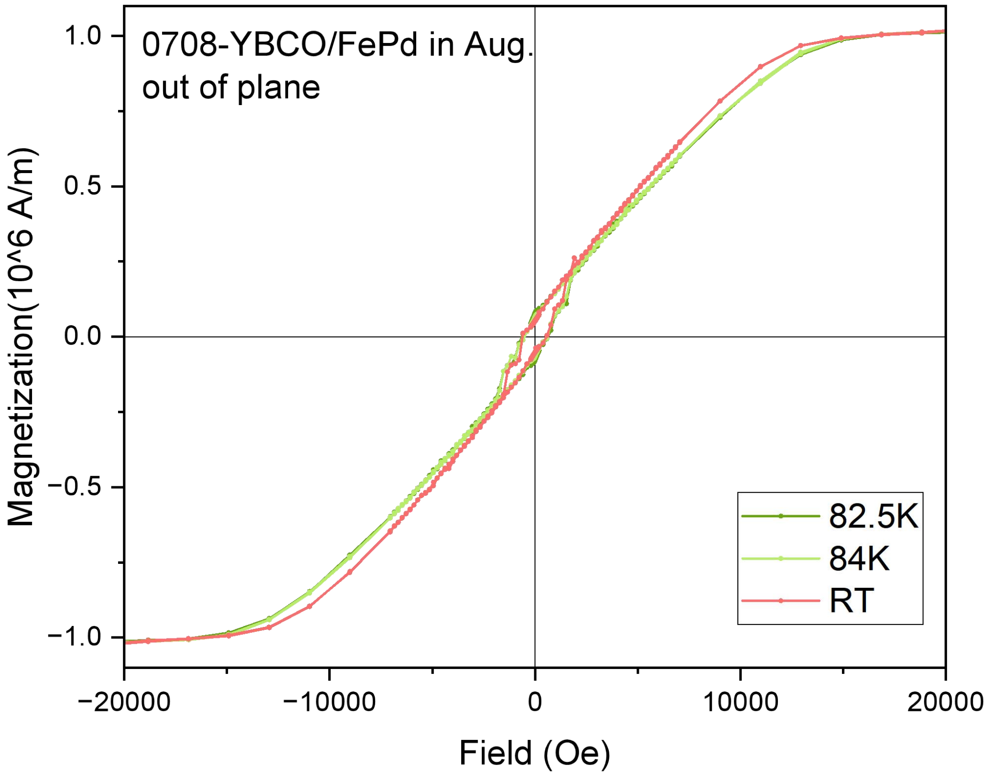

Figure 5.10: M-H curve of sample 0708 at different temperatures in out-of-plane direction. (measured in Aug.)

M-H curves in out-of-plane direction were all measured in August. It can be clearly seen from the Fig.5.9 and Fig.5.10 that the M-H curves in both in-plane and out-of-plane direction measured in the same period vary little with temperature. When the samples are kept in the vacuum chamber for one month and then the same M-H experiments are performed at September in in-plane direction in MPMS, the hysteresis loop shrink slightly and the coercive field becomes slightly smaller. H_C in the in-plane direction in August is around ±70 Oe, while in September it is around ±62 Oe.

5.4 Combined hysteresis loop and magnetoresistance curve

Figure 5.11 shows the R-H loop and the hysteresis loop at a temperature of 89K (T_C=83K). The M-H curve is obtained by MPMS in September at 89K and the applied magnetic field range is ± 5 T. The applied magnetic field needs to be 5 T in order to determine the demagnetization correction curve. The R-H curve is obtained from PPMS measurements in August at 89 K. The applied field range of R-H curve was reduced to ±4000 Oe, to obtain a more detailed curve change.

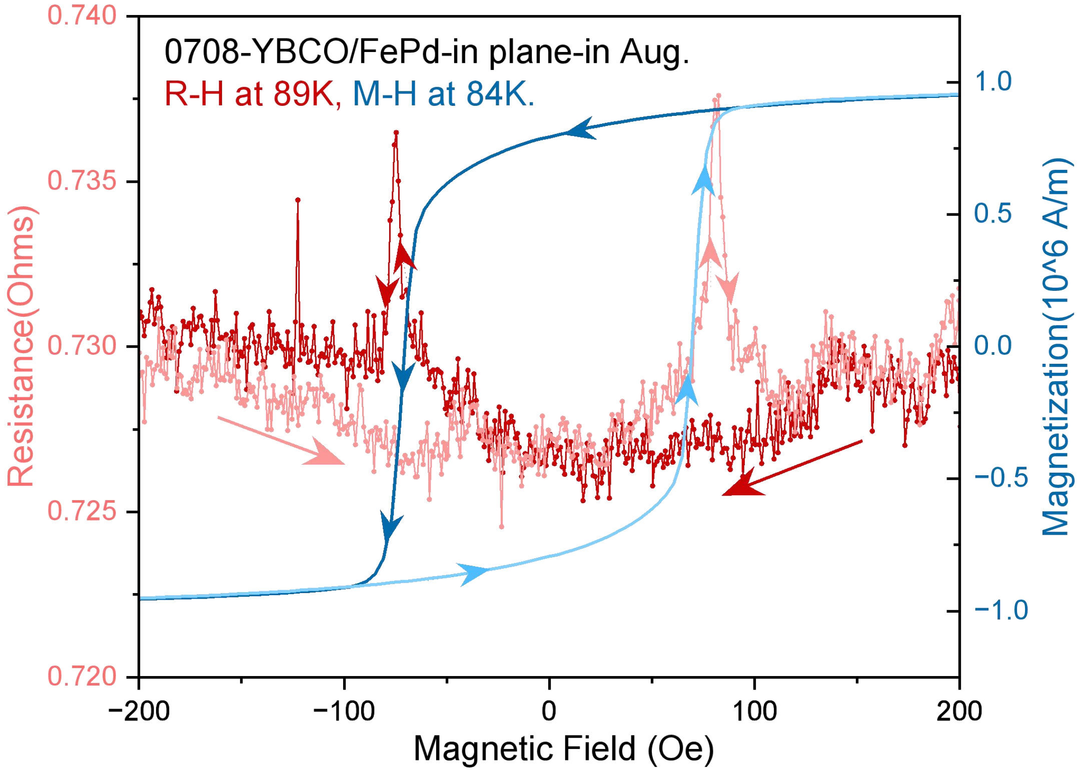

Figure 5.11: Detailed R-H (at 89K) and M-H (at 84K) curves obtained with in-plane magnetization in Aug. 2022 for the sample 0708.

In figure 5.11 it can be clearly seen that the region where the peak of the resistance appears almost coincides with the region of the coercive field in the hysteresis loop. There are a few possible reasons why they do not coincide exactly: First, these samples used to measure R-H and M-H are not identical samples, they are different small pieces of the same sample that have been cut to complete the measurements separately. The cut samples differ in size. Secondly, the measurements of R-H and M-H were not performed at the same temperature - R-H at 89K and M-H at 84K. Finally, the measurements of M-H and R-H curves were done by MPMS and PPMS, respectively, and there are errors in the calibration of different instruments for the applied magnetic field. (Detailed systematic errors of PPMS and MPMS can be found in the appendix 7.3).

The upward peak in R(H) appears after the applied magnetic field is larger than the coercive field H_C in the hysteresis loop. A similar upward peak was measured for the giant magnetoresistance (GMR) effect [26], but the change in resistance in this study was only about 1.5%, not as large as that in the giant magnetoresistance (up to 1600%). The magnetoresistance in GMR appears because there are two ferromagnetic layers with antiferromagnetic arrangement [26], but there is no second ferromagnetic layer in our heterostructure YBCO/FePd, yet the magnetoresistive phenomenon still appears and the upward peaks and coercive field H_C appear in the same applied magnetic field region.

For these upward peaks in resistance near the coercive field in Fig.5.11, there are three possibilities:

First, below the temperature of T_C, the magnetic moment not only penetrates the superconductor, but also the magnetization intensity spreads over a large distance, which is of the order of the superconducting coherence length ξ. The magnetization intensity of FePd suddenly changes direction after the applied electric field exceeds H_C, and the magnetization intensity of the free electrons in FePd at this time is in the opposite direction to that within YBCO. The pairs of electrons with opposite spins form a superconducting condensed state, and they tend to align and the Cooper pairs are broken under the action of the exchange field J in the ferromagnet, so there is a transient rise in resistance [27]. One might argue that this temperature less than T_C precondition cannot be satisfied, because Cooper pairs only exist for $T<T_C$, but these upward peaks in resistance already occur above T_C. However, this could be due to the fact that the strong superconductor fluctuations above the macroscopic transition temperature are not negligible in the under-doped high temperature superconductor [31].

Second, when the magnetization strength M is not uniform in the ferromagnet, a triplet component of the condensed state appears in the superconductor YBCO, which also has a non-zero spin projection. Besides, this triplet state spin can penetrate into the ferromagnetic region in long range. Because of equation 2.10b, the closer the temperature is to T_C, the greater the coherence length will be. As the superconducting condensate penetrates into the ferromagnet, this has a suppressive effect on the superconductivity, which leads to an increase in the resistance, in other words, a decrease in T_C.

Thirdly, near the coercive field, the magnetic domains have the most irregular distribution, which may produce a magnetic moment component perpendicular to the YBCO film, and combined with figure 2.12, it can be seen that CPs can only be formed above the magnetic domains, so the superconductivity is relatively suppressed compared to the state where CPs can be formed in the whole YBCO layer, and a rise in resistance is formed from a macroscopic point of view.

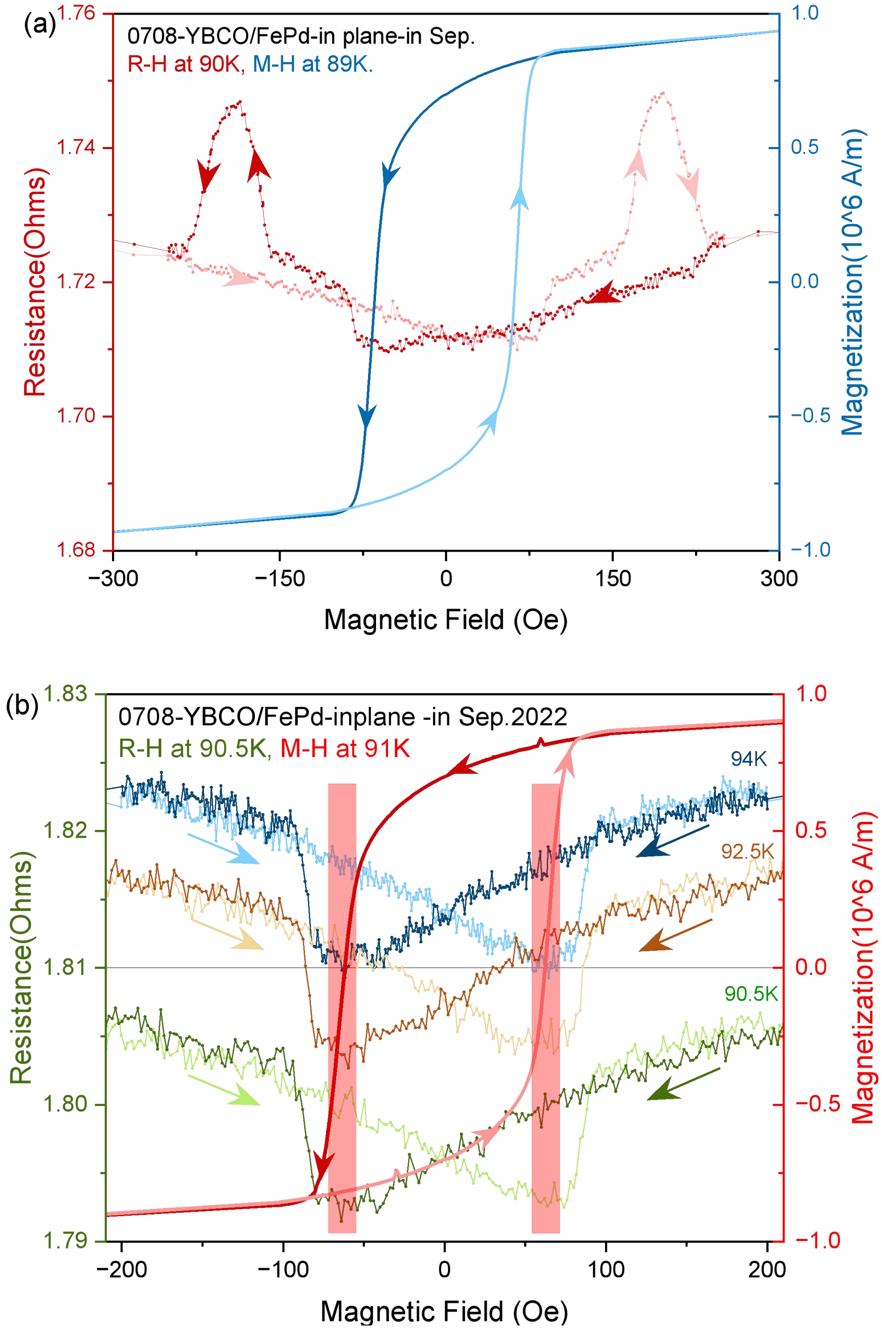

Figure 5.12: (a) Detailed R-H (at 90K) and M-H (at 89K) curves obtained in the in-plane direction in Sep. for the sample 0708. (b) R-H (at 90.5K, 92.5K, 94K) and M-H (at 91K) curves obtained over the SC transition in the in-plane direction in Sep. for the sample 0708.

In order to observe more details of the variation of upward peaks with temperature, the R-H and M-H measurements were performed again in Sep. 2022. Combining R-H and M-H, from figure 5.12 (a), it was found that upward peaks shift toward a larger magnetic field, while downward dips are found near the coercive field due to the shifting of upward peaks. The possible reason for this is that the samples used for the M-H and R-H measurements are not the same piece, and the sample used for the R-H experiments has different H_C in different areas due to the degradation mentioned in appendix 7.2, but this is very hard to observe in M-H curves, while the sample used for the M-H experiments is a well-preserved and undegraded sample, so it is not possible to perfectly detect the coercive field in each area of each sample.

Maybe these dips did not appear in the August measurement due to the coincidence of upward peaks and downward dips in the vicinity of the coercive field. In contrast, the rising peak was relatively larger, so the overall trend was upward. Comparing the R-H in August and September, it is easy to see that the amplitude of the upward peak has also become much larger in Sep.

In Figure 5.12(b), it can be found more intuitively that downward dips can coincide better with the coercive field (red barred area). The possible reason is that similar downward dips appear in the magnetoresistance curve of iron oxide in reference [32], so it can be speculated that a layer of iron oxide appears between YBCO and FePd due to the robbing of oxygen in YBCO by Fe.

Combined with figure 5.6 and 5.7(a), the upward peak appears only in the superconducting transition interval, which is probably due to the fact that: in the non-superconducting transition temperature region, the resistance changes very weakly with temperature as well. The effect of the weakly varying magnetic field energy is also very small when keeping the temperature constant. In the superconducting temperature transition region, the applied magnetic field can have a greater effect on the resistance with a small change in temperature.

5.5 Comparison group of pure YBCO sample 0829

In order to verify if the upward peaks and downward dips in the R-H curves are due specifically to the F/S structure, the ferromagnetic layer FePd was removed from the system, and the same R-H experiments for a pure YBCO sample 0829 were carried out in the PPMS as a control.

As shown in Figure 5.14, no upward peak and downward dip occurred in the in-plane direction, so the sudden change in resistance must be related to a proximity effect in F/S structure. However, in the out-of-plane direction, a positive minimum of about 15 Oe still appears as the applied magnetic field changes from positive to negative, and this minimum does not change as the temperature decreases.

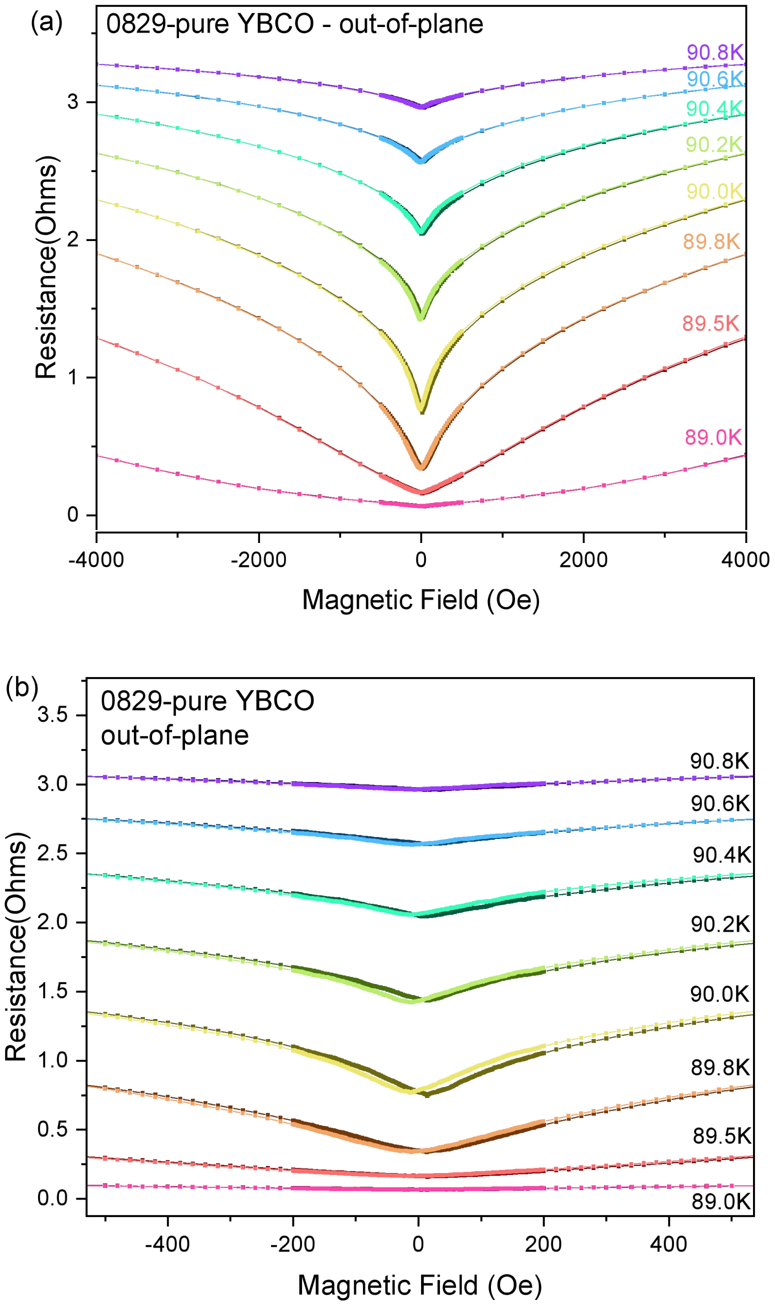

Figure 5.13: Resistance vs. Magnetic Field curves of pure YBCO sample. (b) shows an enlarged detail around zero magnetic field of (a) .

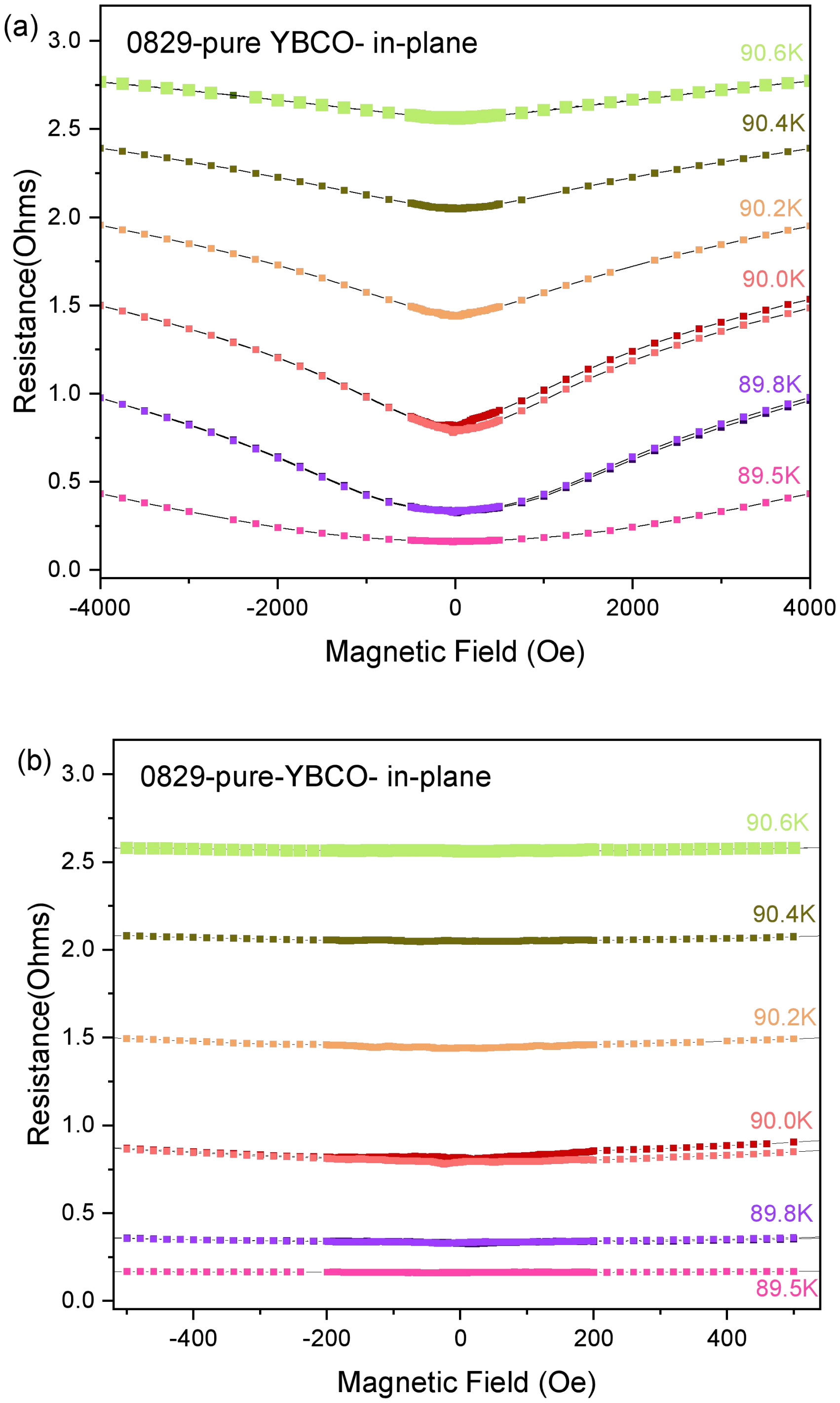

Figure 5.14:Resistance vs. Magnetic Field curves of pure YBCO sample 0829 in the in-plane direction. (b) shows an enlarged detail around zero magnetic field of (a).

In addition, the R-T curves of the same sample 0829 pure YBCO were tested in PPMS at the time before and after the 5-days-long R-H curve measurements as shown in figure.5.15, respectively. Only 5 days were intervened and the sample was always inside the vacuum chamber of PPMS, but the R-T curve showed a left shift due to the highly sensitivity of YBCO to air, that is, under non-high vacuum conditions, the T_C of the pure YBCO sample 0829 became smaller and the superconductivity decreased as the exposure time to air increases.

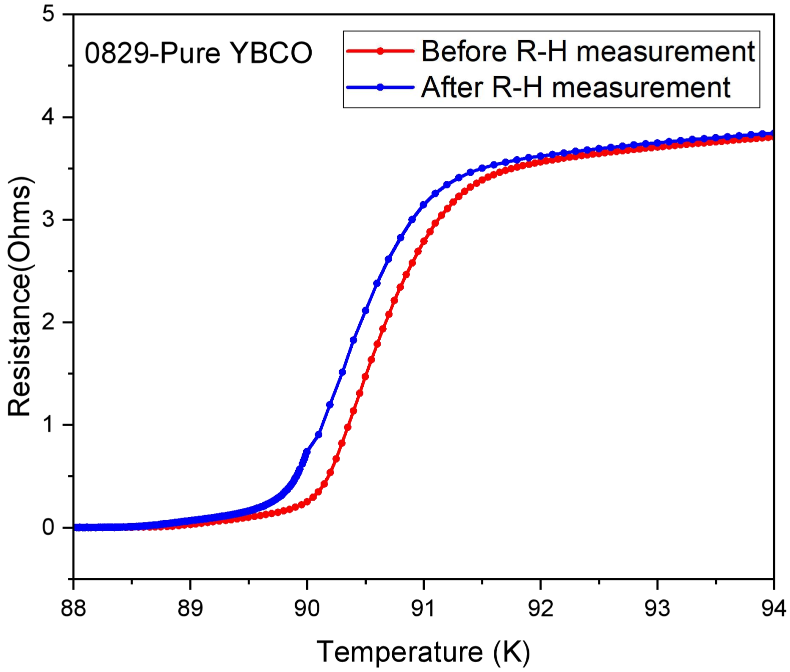

Figure 5.15: Resistance vs. Temperature for the pure YBCO 0829.

5 Conclusions

This project is a complementary study of possible proximity effect in high-temperature superconducting-ferromagnetic ($YBa_2Cu_3O_{7-x}$-FePd) heterostructures based on my project thesis [23]. In the comparison group of my project thesis, FePd film with high PMA were grown with co-depositon at 230℃ on MgO substrate and Pd buffer layer, and FePd film with low PMA could be grown with shuttered-deposition at room temperature. Subsequently, we grew FePd ferromagnetic films with co-deposition and shuttered-depositon on $YBa_2Cu_3O_{7-x}$ high-temperature superconducting films prepared by Prof. Dr. Michael Faley with T_C of about 90 K, respectively. The high-temperature co-deposition method to prepare FePd/YBCO heterogeneous films was discarded, because YBCO loses oxygen in the high-temperature oxygen-free environment, which leads to the degradation of superconductivity.

The in-situ characterization method RHEED was used to monitor the growth process during deposition. From the results of RHEED image analysis, it is known that:

I) The YBCO prepared by sputtering is a single crystal with a rough surface. The high surface roughness is attributed to the nature of YBCO spiral growth.

II) The FePd deposited on the YBCO is polycrystalline. Due to the rough surface of YBCO and its high sensitivity to temperature and oxygen. The inability to provide a flat "substrate" for FePd and the inability to provide sufficient diffusion dynamics at room temperature make it dramatically more difficult to grow $L1_0$-phase FePd by shuttered-deposition, even for low PMA FePd.

Combined with XRD curve analysis:

I) The FePd deposited on YBCO is not $L1_0$-phase, but polycrystalline with columnar growth which is oriented in different directions in the F-layer.

II) FePd/YBCO samples degraded with time, even if they have been stored in the desiccator. Because the system in this study is a metal/oxide system, Fe "steals" oxygen from YBCO.

Combining the R-T and R-H curves, it can be concluded that

I) Applied external field destroys Superconductivity behavior.

II) Superconduting state at lower temperatures requires higher magnetic field to break down.

Combining the R-H and M-H (MFM) curves, it can be concluded that

I) The easy magnetization axis of FePd/YBCO samples are in the in-plane direction and the magnetic domains are oriented in the in-plane direction.

II) H_{C2} of YBCO decreases with increasing temperature.

III) In fresh FePd/YBCO sample in Aug. 2022, the properties of YBCO superconducting films are suppressed in the in-plane direction, close to the coercive field. This might be due to 1) the breaking of Cooper pairs, 2) Domain wall superconductivity, 3) or because of the appearance of reversed parallel aligned magnetic moments within the superconducting- and ferromagnetic layers.

IV) R-H curves were remeasured in Sep. 2022, downward dips appeared near the coercive field in the in-plane direction, probably due to FePd stealing the oxygen from YBCO and from the iron oxide layer in between. The upward peaks flattened out to a larger magnetic field, possibly due to partial YBCO degradation, which leads to a corresponding change of H_C in different regions.

V) Upward peaks appear only in the superconducting transition interval, which is probably due to the fact that: in the non-superconducting transition temperature region, the resistance changes very weakly with both temperature and external magnetic filed. So when the temperature is kept constant and only a small magnetic field changed, it is difficult to observe a large change in resistance macroscopically.

In the out-of-plane direction:

A deviation of about 10Oe is observed in both the F/S and pure YBCO samples, probably due to PPMS offset.

6 Outlook

The F/HTS (FePd/YBCO) system in this study is different from most existing systems in the literature, as it is an in-plane system. This is shown by the fact that for the ferromagnetic layer, the easy magnetization axis is along the in-plane direction and the magnetic domains are also completely in-plane. For the superconducting layer, the conductivity is also in the in-plane direction (along the CuO_2 chain).

Due to the high sensitivity of YBCO to oxygen, the presence of Fe in the F-layer is certainly a great difficulty to overcome. Transforming the system F/S from metal/oxide to oxide/oxide might be a worthwhile direction to go deeper, so that the problem of interaction between Fe and oxygen can be successfully solved and thus proximity effects in an all oxide system can be investigated.

An epitaxial ferromagnetic layer with high perpendicular magnetic anisotropy (HPMA) could be grown on the YBCO (HTS layer). In the proximity effect, magnetic domains in the out-of-plane direction have a more pronounced effect on the S-layer compared to the in-plane ones.

Grazing incident small-angle neutron scattering (GISANS) and polarized neutron reflection (PNR) are used to obtain more information about the interface magnetism and structure. In addition, PNR can be used to detect the O content in YBCO and further investigate the T_C and structural changes of YBCO at the interface.

7 Appendix:

7.1 Sample preparation for PPMS

1. Firstly, the samples containing YBCO films are glued to the rotating sample holder using double-sided tape to ensure the stability of subsequent connections.

2. Wipe the surface of the indium wire with a cotton swab dipped in acetone to remove impurities, followed by cutting the metallic platinum into small 1-1.5 mm sections using a knife, as in Figure 1a.

3. Use clean flat forceps to press the small pieces of indium onto the sample surface and the connecting channel respectively, and make sure that the indium does not move on the sample and the channel, as in Figure 1b. Note that the indium should not exceed the metal zone of the channel on the sample holder, and if it does, the excess indium needs to be cleaned off with a knife.

4. Cut the silver wire with scissors to the appropriate length, i.e., to be able to connect the channel on the sample holder to the sample with an appropriate margin.

5. Press the ends of the silver wire onto the indium points on the channel and sample and the press some new indium pieces on the silver wire until the contact is firm. The complete connection is shown in Figure 2.

6. Measure the resistance between each two channels on a resistance meter. A total of six sets of four channels need to be tested to ensure that there is resistance between each two points, i.e. a good connection.

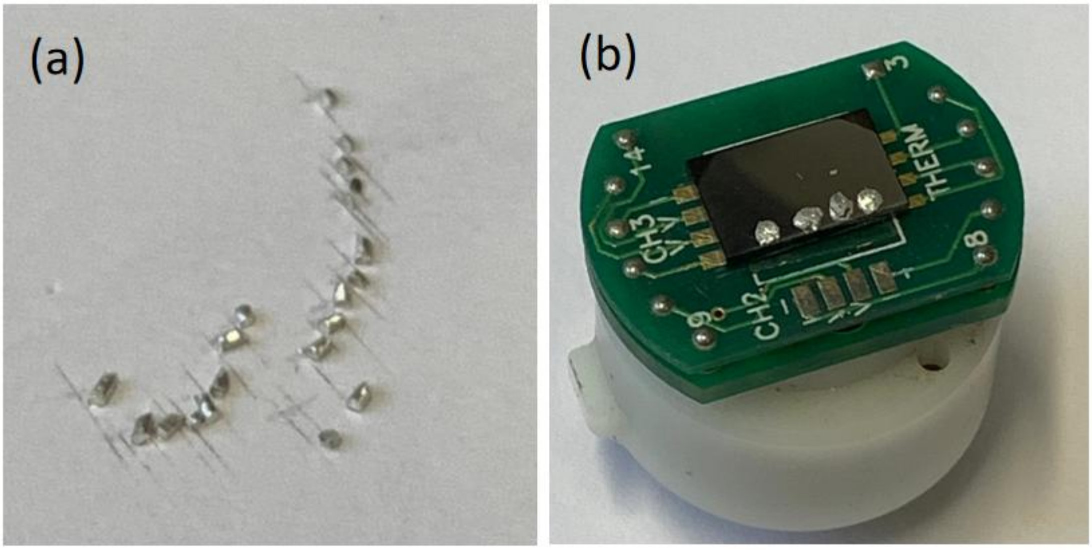

Figure 7.1: (a) small pieces of indium. (b) indium spot on the sample surface.

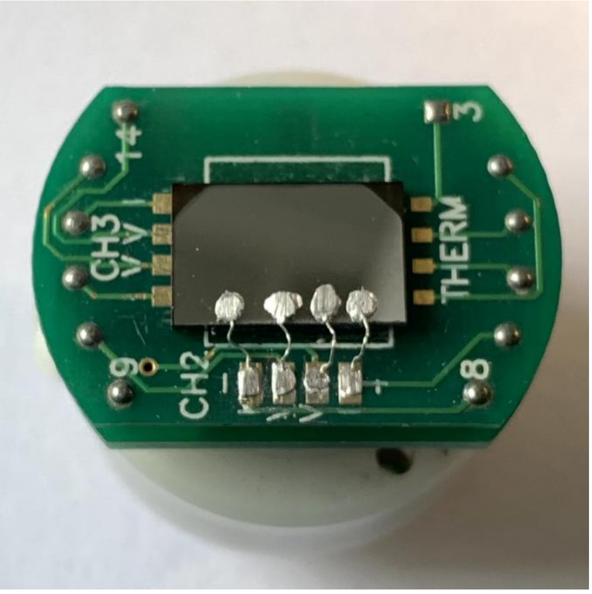

Figure 7.2: complete good connection of sample F/S.

7.2 sample degradation

Figure 7.3 shows the samples that were left in the vacuum box for 6 months after the PPMS experiment. The sample superconductivity was partially degraded due to condensate water adhering to the sample near the indium point during the removal of the sample from the PPMS chamber. This has a significant impact on the reproducibility of the experiment, as evidenced by the collective increase in the resistance of the sample. When temperature is below the T_C, the resistance is not near zero. The uneven area near the indium point in figure 7.3 is the degraded area.

Figure 7.3: a partially degraded sample.

7.3 PPMS & MPMS offset

By using the fluxgate, the residual field at PPMS was measured to be +5.55Oe after a hysteresis measurement by the user before. After settle down from 3T in oscillating mode we measured less than +2.5Oe.

The deviation in magnetic field for MPMS is +0.23Oe. It seems the MPMS low field option has a problem. By a field compensation, the system doesn't finish and iterates permanently. It should be better than 0.1Oe. Perhaps the Power supply shows a ripple or isn't constant.

Thanks to PD Dr. Oleg Petracic for teaching me about field error measurement using fluxgate, and many thanks to Berthold Schmitz for his patience and help in measuring PPMS and MPMS offsets.

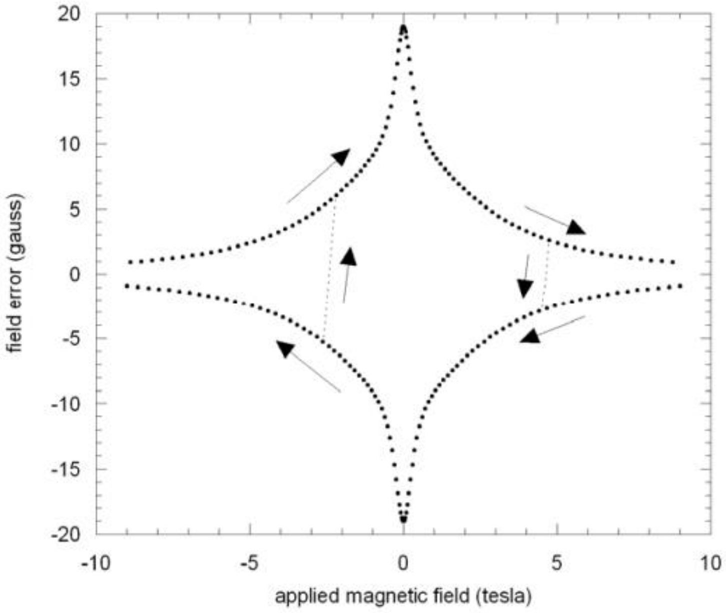

Figure 7.4: Field error vs. the charge field in a typical 9 tesla PPMS magnet. The figure is taken from [30].

References:

[1] D. Weller and A. Moser, “Thermal effect limits in ultrahigh-density magnetic recording”. IEEE Transactions on Magnetics, 35(6): 4423-4439, Nov. 1999.

[2] A. Hubert and R. Schafer, “Magnetic Domains The Analysis of Magnetic Microstructures”. Springer, 107–354, 2000.

[3] Annika Stellhorn, “Tailoring superconducting states in superconductor-ferromagnet hybrids”. New J. Phys. 22(093001), 2020.

[4] David Jiles, “Introduction to Magnetism and Magnetic Materials”. Engineering & Technology, Physical Sciences, 2015.

[5] Kittel, C. “Introduction to Solid State Physics”. New York, 1986.

[6] S.Chikazumi, Physics of Magnetism, John Wiley & Sons, New York, 1964.

[7] M.I. Darby and E.D. Isaac, “Magnetocrystalline anisotropy of ferro- and ferrimagnetics”. IEEE Transaction on Magnetics, 10(2): 259-304, June 1974.

[8] Chaisak Issro, Madjid Abes, Wolfgang Puschl, etc. “Atomic Ordering and Magnetism in $L1_0$ Ordered FePd Alloys”, Metallurgical and Materials Transactions A, 37A: 3415, Dec. 2006.

[9] Mitsuru Ohtake, Shouhei Ouchi, Fumiyoshi Kirino, etc. “$L1_0$ ordered phase formation in FePt, FePd, CoPt, and CoPd alloy thin films epitaxially grown on MgO(001) single-crystal substrates”. Journal of applied physics, 111: 07A708, 2012.

[10] V. V. Schmidt, “The Physics of Superconductors: introduction to fundamentals and applications”, Springer, 1997.

[11] Zhaorong Yang, Martin Lange, Alexander Volodin, etc. “Domain-wall superconductivity in superconductor – ferromagnet hybrids”, Nature materials, Vol.3, Nov. 2004.

[12] Annette Bussmann-Holder, Hugo Keller, “High-temperature superconductors: underlying physics and applications”, De Gruyter: 1-12, 2019.

[13] Chris Safranski, “Resistance of the Superconducting Material YBCO”, a Senior Project, California Polytechnic State University, 2010.

[14] V. Breit, P. Schweiss, R.Hauff, H.Wuehl, etc. “Evidence for chain superconductivity in near-stoichiometric $YBa_2Cu_3O_x$ single crystals”. Physical Review B, 52(22): 727-730, Dec. 1995.

[15] J. Reichow. “Technical System Description of DCA MBE M600 Molecular Beam Epitaxy System”. Jan. 2010.

[16] Fernando Rinaldi, “Basics of Molecular Beam Epitaxy (MBE)”. Annual Report, University of Ulm, 2002.

[17] Sakamoto, T. “Physics, Fabrication, and Applications of Multilayered Structures”, NATO Science Series B, 182: 93-110, 1988.

[18] R. L. Fagaly. “Superconducting quantum interference device instruments and applications”. Review of Scientific Instruments, 77: 101101, 2006.

[19] Y. Kinoshita, T. Miyakawa, X. Xu. “Long-distance polarizing microscope system combined with solenoid-type magnet for microscopy and simultaneous measurement of physical parameters”. Rev. Sci. Instrum, 93: 073702, 2022.

[20] Annika Stellhorn, “Tailoring superconducting states in superconductor-ferromagnet hybrids”, New J. Phys, 22: 093001, 2020.

[21] CrysTec. “Data-Sheet of MgO substrate”.

[22] M. I. Faley, D. Meertens, U. Poppe and R. E. Dunin-Borkowski “Graphoepitaxial high-Tc SQUIDs”, Journal of Physics, Conference Series (507): 042009, 2014.

[23] Mengying Tang, “Study of microstructural, magnetic and electrical transport properties in YBCO/FePd heterostructures”, project thesis RWTH, 2022.

[24] Jianwei Ye, “Investigation of the Domain Structure of FePd Thin Film”, master thesis RWTH, 2020.

[25] V. V. Balashev and V. V. Korobtsov, “Structure of Ultrathin Polycrystalline Iron Films Grown on SiO2/Si(001)”. Technical Physics, 63(1): 73 – 77, 2018.

[26] V. Pena, Z. Sefrioui, D. AriasGiant, etc. “Magnetoresistance in Ferromagnet/Superconductor Superlattices”. Physical Review Letters, 94: 057002, 2005.

[27] F.S.Bergeret, A.F.Volkov and K.B.Efetov. “Induced ferromagnetism due to superconductivity in superconductor-ferromagnet structures”. Physical review, B69: 174504, 2004.

[28] Jinkwan Kwoen and Yasuhiko Arakawa. “Classification of Reflection High-Energy Electron Diffraction Pattern Using Machine Learning”, Crystal Growth and Design, 20(8): 5289-5293,

2020.

[29] Michael Faley, “Multilayer buffer for high-temperature superconductor devices on MgO”. Applied Physics Letters, 89: 082507, 2006.

[30] Quantum Design Application, Rev: A0, 2009.

[31] J. Stahn, J. Chakhalian, Ch. Niedermayer, ect. “Magnetic proximity effect in perovskite superconductor/ferromagnet multilayers”. Physical Review, 71: 140509, 2005.

[32] Jolanta Stankiewicz, Félix Jiménez-Villacorta, and Carlos Prieto. “Magnetotransport properties of oxidized iron thin films”. Physical Review B, 73: 014429, 2006.

[33] Quantum design. “Physical Property Measurement System Hardware Manual”.

7 Acknowledgements

I finished master thesis at JCNS-2 / PGI-4/ PGI-5 in Forschungszentrum Jülich (FZJ) during the last one year. I would like to sincerely thank all my colleagues and supervisors who have helped and supported me.

Many thanks to Prof. Dr. Thomas Brückel for providing me this wonderful opportunity to work at JCNS-2 and supporting my work.

Many thanks to Prof. Dr. Joachim Mayer for reviewing my thesis as the examiner.

Many thanks to Dr. Emmanuel Kentzinger, Dr. Connie Bednarski-Meinke, Prof. Dr. Michael Faley, Dr. Mai Hussein and Vitor Alexandre, de Oliveira Lima for all the support, discussions and many useful suggestions every weeks.

Many thanks to Dr. Emmanuel Kentzinger, Dr. Connie Bednarski-Meinke, Dr. Mai Hussein and Vitor Alexandre, de Oliveira Lima for your time and effort in helping me prepare for my pre-defense and for your great suggestions for revisions.

Many thanks to Dr. Connie Bednarski-Meinke for help and patience with operation of AFM, MFM and OMBE.

Many thanks to Prof. Dr. Michael Faley for perparing all YBCO samples and taking SEM, TEM images to support our work.

Many thanks to Dr. Annika Stellhorn and Msc. Jianwei Ye for providing her/his experience and lots of suggestions on optimized growth parameters of the OMBE system.

Many thanks to PD Dr. Oleg Petracic, Dr. Shibabrata Nandi and Dr. Ulrich Rücker for the safety instructions on the MPMS system, the PPMS system and the X-ray lab.

Many thanks to Berthold Schmitz for helping me solve problems in using the PPMS, MPMS and DynaCool systems.

Many thanks to Dr. Lei Cao, Yifan Xu and Chenyang Yin for teaching me deal with the XRR data and the operation of the XRD instrument.

At last I would like to especially thank my parents and friends for their love and support.